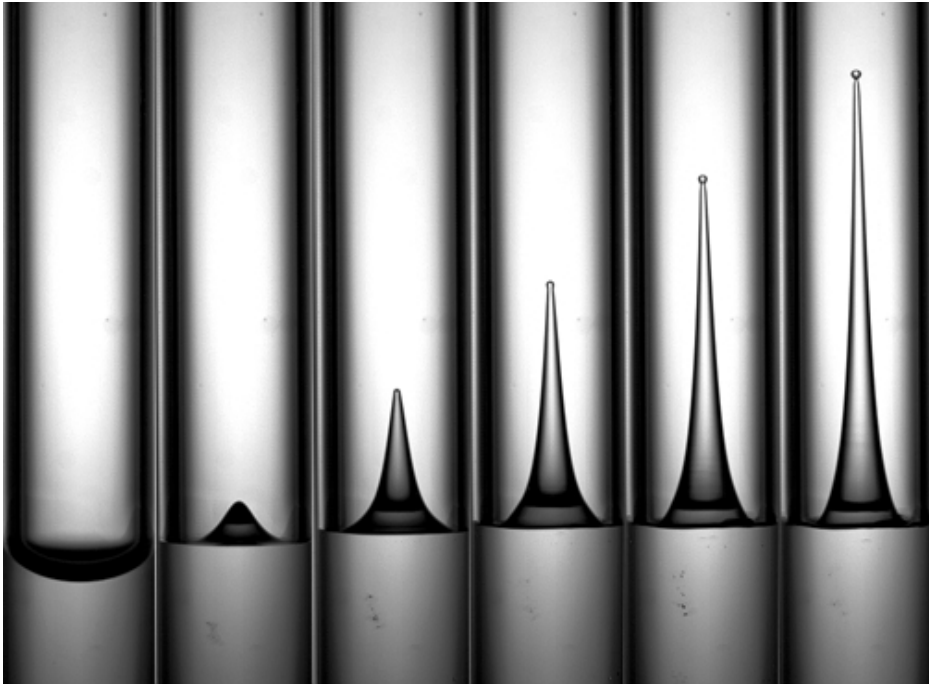


# Tubular jet generation by pressure pulse impact



## Master thesis

Gerben Morsink

*Graduation Committee:*

Prof. Dr. D. Lohse

A. Klein, MSc.

Dr. S. Kooij

Dr. C. Sun

*Physics of Fluids Group, Faculty of Science and Technology,  
University of Twente, 7500 AE Enschede, The Netherlands*

**December 23, 2011**



## Abstract

The formation of highly focused thin jets caused by impact of a pressure pulse on a free surface is studied experimentally. Jets with a tip speed up to  $50 \text{ m s}^{-1}$  are measured. The pressure pulses generated by an eddy-current actuator have a duration of about  $100 \mu\text{s}$  and reach a peak amplitude of over 100 bar. The pressure pulses travel upwards through an ultrapure water column in a rigid steel tube of 1 m length at approximately the speed of sound. The pressure is measured using two pressure sensors working at 20 MHz. A glass tube of 2 mm to 4 mm in radius is inserted at the top of the steel tube, to enable visualisation of the free surface and the jet formation following the impact of the pressure pulse. These images are analysed to study the effect of the experimental parameters on the jet velocity of the jet tip: amplitude of the pressure pulse, initial curvature, and tube diameter<sup>1</sup>. The amplitude of the pressure pulse is shown to have a linear relation with the velocity of the jet tip. The initial curvature of the free surface, or meniscus, ranged from highly concave to slightly convex and is shown to be an important aspect in the formation of the jet, which can be described by one parameter: the contact angle ( $\theta_c$ ). It is shown that the tip speed is proportional to  $\cos\theta_c$ . A combination of linear acoustic theory with the contact angle dependency leads to good agreement with the measurements. It is shown that the speed of the tip of the jet does not depend on the tube radius.

---

<sup>1</sup>To be submitted to the Journal of Fluid Mechanics as: *Tubular jet generation by pressure pulse impact.*



**Contents**

|  |           |
|--|-----------|
| <b>1. Introduction</b>   | <b>1</b>  |
| <b>2. Theory</b>   | <b>3</b>  |
| 2.1. Distinction between jets . . . . .                        | 3         |
| 2.2. Contact angle dependency on tip speed . . . . .           | 4         |
| 2.2.1. Meniscus shape . . . . .                                | 4         |
| 2.2.2. Focusing effect . . . . .                               | 6         |
| 2.3. Effect of pressure on tip speed . . . . .                 | 8         |
| 2.4. Jet Breakup . . . . .                                     | 10        |
| 2.5. Potential flow and boundary integral theory . . . . .     | 10        |
| <b>3. Experimental setup</b>                                   | <b>12</b> |
| 3.1. The shocktube experiment . . . . .                        | 12        |
| 3.2. Eddy current actuator . . . . .                           | 12        |
| 3.3. Pressure sensors . . . . .                                | 15        |
| 3.3.1. Fiber Optic Probe Hydrophone (FOPH) . . . . .           | 16        |
| 3.3.2. PVDF piezoelectric pressure sensors . . . . .           | 16        |
| 3.3.3. Comparison of FOPH and PDVDF pressure sensors . . . . . | 17        |
| 3.4. Glass tubes . . . . .                                     | 17        |
| 3.4.1. General tubes . . . . .                                 | 17        |
| 3.4.2. Coated tubes . . . . .                                  | 18        |
| <b>4. Experimental results and Discussion</b>                  | <b>19</b> |
| 4.1. General results . . . . .                                 | 19        |
| 4.2. Effect of pressure pulse amplitude on tip speed . . . . . | 23        |
| 4.3. Effect of contact angle on tip speed . . . . .            | 25        |
| 4.4. Effect of tube radius on tip speed . . . . .              | 27        |
| <b>5. Future work</b>  | <b>29</b> |
| <b>6. Conclusion</b>   | <b>30</b> |
| <b>References</b>  | <b>32</b> |
| <b>A. Appendix</b>   | <b>35</b> |
| A.1. Boundary integral simulations . . . . .                   | 35        |
| A.2. Side experiments and possible future projects . . . . .   | 36        |
| A.2.1. Higher Bond numbers . . . . .                           | 36        |
| A.2.2. Flat free surface . . . . .                             | 37        |
| A.2.3. A convex free surface . . . . .                         | 37        |
| A.2.4. Ring jet formation . . . . .                            | 39        |
| A.2.5. Small air bubbles at the free surface . . . . .         | 43        |

## Contents

---

|  |    |
|--|----|
| A.2.6. A big air bubble beneath the free surface . . . . . | 44 |
| A.2.7. Tiny droplets . . . . .                             | 45 |
| A.3. Schlieren Setup . . . . .                             | 45 |
| A.3.1. Light sources . . . . .                             | 45 |
| A.4. Cleaning method . . . . .                             | 48 |

List of Figures

|     |   |    |
|-----|---|----|
| 1.  | Four examples of liquid jets. . . . .   | 1  |
| 2.  | Schematic drawing of a meniscus . . . . .   | 5  |
| 3.  | Schematic diagram of the experimental setup . . . . .   | 13 |
| 4.  | Experimental relation between electrical energy input $E_{el}$ , voltage $U_C$ and maximum pressure $P_{max}$ . . . . .   | 14 |
| 5.  | Comparison of a single pressure record acquired simultaneously by a FOPH and a PVDF pressure transducer, and mean pressure record of 100 shots with the PVDF sensor. . . . .        | 18 |
| 6.  | Image sequence of a typical experiment . . . . .  | 20 |
| 7.  | Digitally processed image sequence of figure 6 . . . . .  | 21 |
| 8.  | Speed of the jet tip, $v_{tip}$ , and lowest meniscus point at the very beginning of the jet formation, $v_{meniscus}$ , plotted against time $t$ for four input voltages . . . . . | 21 |
| 9.  | Volume flow, $\dot{V}$ , and flow speed, $v_{flow}$ , at different positions $z_i$ along the jet plotted against time $t$ for the jet evolution shown in figure 6 . . . . .         | 22 |
| 10. | Simultaneous pressure record of two PVDF pressure transducers at different positions during the jet creation shown in figure 6. . . . .   | 23 |
| 11. | Comparison of the experiment from this thesis with theory for the relation of contact angle and tip speed . . . . .   | 24 |
| 12. | Image sequence with a non-zero contact angle . . . . .  | 25 |
| 13. | Image Sequence with a lower non-zero contact angle, compared to figure 12 . . . . .   | 26 |
| 14. | Image Sequence with an even lower non-zero contact angle, compared to figure 12 and figure 13 . . . . .   | 26 |
| 15. | Comparison of experiments and theory for the relation of the contact angle with the tip speed . . . . .   | 27 |
| 16. | Digitally processed image sequence of figure 6 with the shape evolution from BI simulations. . . . .  | 35 |
| 17. | Jet in a big tube . . . . .   | 36 |
| 18. | Schematic drawing of the dision of a higher bond number meniscus in two parts. . . . .  | 37 |
| 19. | Image sequence of a flat surface that creates a singular jet in the second stage of meniscus development. . . . .   | 38 |
| 20. | Image sequence of jet generation with a convex menisucs. . . . .  | 40 |
| 21. | Image sequence that shows ring jet formation. . . . .   | 41 |
| 22. | Simultaneous pressure record of two PVDF pressure transducers at different positions. . . . .   | 42 |
| 23. | Schematic diagram of the experimental setup with the points of reflection. . . . .  | 43 |
| 24. | Image sequence with a small bubble. . . . .   | 44 |
| 25. | Image sequence of a jet created inside a big bubble several centimeter below the surface. . . . .   | 46 |

## List of Figures and list of tables

---

|     |   |    |
|-----|---|----|
| 26. | Image sequence where tiny droplets are created. . . . . | 47 |
| 27. | Experimental Schlieren setup. . . . .                   | 47 |
| 28. | Schematic drawing of the light source. . . . .          | 48 |
| 29. | Different cleaning methods. . . . .                     | 48 |

## List of Tables

|    |   |    |
|----|---|----|
| 1. | Parameter range and dimensionless numbers of the experiment. . . .  | 4  |
| 2. | Wire and coil characteristics . . . . .   | 15 |
| 3. | Values of mean tip speed for $0^\circ$ contact angle, two different voltages<br>and two tube radii. . . . . | 28 |
| 4. | The rms and peak-peak values for the three differently treated mi-<br>croscope slides. . . . .              | 48 |





## 1. Introduction

Liquid jets are collimated streams of liquid matter that emerge from a liquid-gas interface. Jets of sea water are accountable for the production of sea salt aerosols, by launching droplets from the sea surface (Monahan & Mac Niocaill, 1986). A less common example of jets occurs in human medicine: in order to prevent a full medical surgery, the lithotripsy procedure uses shockwaves that create focused jets that emerge from air cavities close to kidney stones to destroy them (Zhu *et al.*, 2002). Unwanted appearances of jets in human medicine occur for example during ultrasound treatments, which can result in lesions in the lungs or other tissue (O'Brien Jr., 1998). Liquid jets are also one of the reasons of cavitation damage near solid surfaces, for example damage to ship propellers (Young, 1989; Blake & Gibson, 1987). By using a concave shaped liquid-gas interface that resembles the lower half of a bubble, focused jets will eject from this interface. An example of the application of focused liquid jets occurs in inkjet printers, when printing a document. A concave surface is also used to deliberately produce fast jets by shaped charges (Walters & Zukas, 1989). Figure 1 shows different jets, created by different mechanisms. A list of authors in the field of liquid jets can be found in the bibliography of the paper by Eggers & Villermaux (2008).

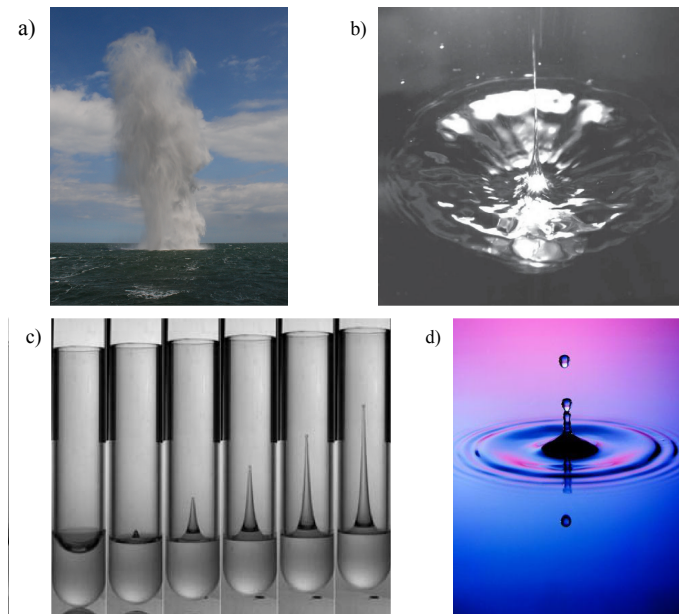


Figure 1: Four examples of liquid jets created by a) the explosion of an underwater mine ([www.manw.nato.int](http://www.manw.nato.int)), b) pulling a circular disc down through an air/liquid interface (Gekle & Gordillo, 2010), c) a bouncing tube (Antkowiak *et al.*, 2007), d) the impact of a water droplet in a water bath (Science Photo Library). Although different generation mechanisms are involved, all are liquid jets and exhibit the features discussed in this report.

## 1. Introduction

---

Jet formation caused by various mechanisms is studied in many papers (e.g., Duchemin *et al.*, 2002; Lin & Reitz, 1998; Gekle & Gordillo, 2010). The breakup of jets was already studied in the 19<sup>th</sup> century by Lord Rayleigh, and Plateau (Rayleigh, 1879; Plateau, 1873). One way to create a liquid jet is by hitting a bubble with a pressure pulse. Free bubbles are often small and mobile. Therefore, they are not very suitable to obtain reproducible results in an experimental setting. The mechanism described in this report to create jets is by generating a pressure pulse at the bottom of a tube, after which the pulse moves up through a liquid column to a free surface. The words free surface and meniscus are used interchangeably. If a small, hydrophilic tube is used, then a meniscus whose surface exhibits the same shape as the lower half of a bubble will be created. These shocktube experiments are conducted to study how changes in pressure and contact angle affect the liquid jet. The results of this study can be used to improve efficiency in existing systems or to create new applications. Future applications are for example needle-free injection by generating a fast, micro-sized focused jet, or a new jet injection system in engines with a higher energy efficiency (Oudalov, 2011).

At the start of this thesis, the shocktube setup was used to investigate the negative pressure of the reflected pressure pulse (Morsink, 2010). Many authors mention the shocktube experiment as a way to investigate the negative pressure regime (e.g. Caupin & Herbert, 2006; Greenspan & Tschiegg, 1982; Herbert *et al.*, 2006). One of the first shocktubes used an explosive to generate the pressure pulse. In later shocktube setups, the explosive is replaced by a piston-bullet combination, where a bullet is shot against a piston (Temperley & Trevena, 1979; Williams & Williams, 2002). Preliminary measurements showed that the shocktube experiment generates reproducible jets. The results of these measurements changed the focus of this thesis towards jet formation.

High-speed cameras are used to capture the jet formation and evolution and high-speed pressure sensors are used to measure the characteristics of the pressure pulse. The experiments described in this thesis will contribute to a better understanding of the jet formation. Section 2 describes how the tip speed is expected to be affected by an increase in pressure and change in contact angle. As a model for the relation between tip speed and pressure the particle velocity from linear acoustic theory is used (Kedrinskii & Translated by Svetlana Yu. Knyazeva, 2005; Reynolds, 1981). Two models are compared with a different description of the focusing effect, which relates curvature to the tip speed. A different approach to model jet formation is by using numerical simulations. Simulations based on the boundary integral method are compared with the experimental results (Gekle *et al.*, 2009; Peters, 2011). The experimental setup that is used is described in chapter 3. The results are shown in chapter 4. Results from this experiment indicate a need for further research into the effect of small contaminants on jet formation, next to the need of visualizing (reflections of) the pressure pulse and cavities in the liquid column. Other possible future work and a conclusion are found chapter 5 and 6, respectively. Side experiments will be addressed in the appendix (A.2) of this report.

## 2. Theory

Section 2.1 discusses what characteristics we used to describe our jet. Several effects play a role when the tip speed of the jet is regarded. Two of them will be discussed: the first is the focusing effect of the meniscus shape (section 2.2), the second is influence of the pressure pulse amplitude (section 2.3). Finally, the incompressible, axisymmetric boundary integral model that is compared with the experiments is discussed.

### 2.1. Distinction between jets

In the experiments where a sphere or disc hits the liquid and in explosion experiments, an air or vapour cavity, is created under the liquid surface during the experiment. An air or vapour cavity is absent in experiments with a bouncing, liquid-filled tube. Therefore presence of an air cavity could be used to distinguish between types of jets. Another distinction of types of jets is between liquid jets created in tubes or in a bath. Whereas tubular jets do in general not have a flat free surface and the walls have an influence on the jet formation, jets created in a liquid bath stem from a free surface that is in general flat and feel no influence of walls. The shape and speed of the jet changes with the curvature of the free surface, because of the focusing effect that occurs with a concave-shaped free meniscus.

Another distinction between different types of jets can be made when the most important forces that create the jet are characterised. This can be done with the help of dimensionless numbers. The values of the important dimensionless numbers for our experimental setting are given in table 1. The Weber number measures the relative importance of the fluid's inertial force compared to its surface tension force,

$$We = \frac{\rho v_{\text{tip}}^2 R}{\sigma}. \quad (1)$$

It is an important number in studies of jet formation, because it is used to describe processes that are dominated by the surface tension force, such as droplet formation and breakage of liquid jets (Gekle *et al.*, 2009; Gekle & Gordillo, 2010). If  $We \gg 1$ , this means that inertial forces are dominant over surface tension forces. Another example of the use of the Weber number is found in inkjet printing, where  $We \approx 4$  is the boundary between the dripping and jetting regime (van Hoeve *et al.*, 2010).

The Reynolds number gives the ratio of inertial forces to viscous forces,

$$Re = \frac{\rho v_{\text{tip}}^2 R^2}{\mu v_{\text{tip}} R} = \frac{\rho v_{\text{tip}} R}{\mu}, \quad (2)$$

where  $Re \gg 1$  means that inertial forces are dominant over viscous forces. The Froude number is a dimensionless number defined as the ratio of inertial force to gravitational forces,

$$Fr = \frac{v_{\text{tip}}^2}{gR}, \quad (3)$$

## 2. Theory

---

where  $Fr \gg 1$  means that inertial forces are dominant over gravitational forces. In our experiment the height of the camera view is of the same order as the width of the tube. Therefore a high Froude number means that while recording the jet, the influence of gravity is negligible. The Froude number is defined in such a way in this work, that

$$Bo = \frac{We}{Fr} = \frac{\rho g R^2}{\sigma}. \quad (4)$$

The Bond number is a measure of the importance of surface tension forces compared to the gravitational body force. It is an important quantity to describe the initial static situation, but not for describing the evolution of the jet, because it involves no dynamic quantity like  $v_{\text{tip}}$ . However, as will be discussed in section 2.2, the initial meniscus shape does influence the evolution of the jet. It turns out to be a handy measure of the importance of gravity on the meniscus shape, because it is the squared ratio of the tube radius  $R$  with the capillary length  $\lambda_c$ ,

$$\lambda_c = \sqrt{\frac{\sigma}{\rho g}}, \quad (5)$$

where  $Bo < 1$  means that  $R < \lambda_c$  and that the meniscus shape is part of a circle<sup>2</sup>.

|                              |                | Minimum value     | Maximum value     |
|------------------------------|----------------|-------------------|-------------------|
| <b>Control parameters</b>    | R [mm]         | 2                 | 4                 |
|                              | $\theta_c$ [°] | 0                 | 90                |
|                              | $U_C$ [V]      | 800               | 2400              |
| <b>Dimensionless numbers</b> | $Bo$           | 0.5               | 2.5               |
|                              | $We$           | $1.0 \times 10^2$ | $1.5 \times 10^5$ |
|                              | $Re$           | $8 \times 10^3$   | $2 \times 10^5$   |
|                              | $Fr$           | $2 \times 10^2$   | $3 \times 10^5$   |

Table 1: Parameter range and dimensionless numbers of the experiment. Control parameters include the tube radius ( $R$ ), contact angle ( $\theta_c$ ) and voltage of the capacitor bank ( $U_C$ ). Dimensionless numbers include Bond number ( $Bo$ ), Weber number ( $We$ ), Reynolds number ( $Re$ ), and Froude number ( $Fr$ ). The dimensionless numbers are based on the control parameters and the measured speed of the tip of the jet. The tip speed ranged from  $2 \text{ m s}^{-1}$  to  $50 \text{ m s}^{-1}$ . Under a given pressure limit, no jet is observed at all, only a slight deformation of the surface. The minimum jet speeds is therefore the slowest jet that is observed.

## 2.2. Contact angle dependency on tip speed

### 2.2.1. Meniscus shape

The shape of the free surface, or meniscus, plays an important role in the jet formation. As long as the meniscus is axisymmetric, the shape of it can be uniquely

---

<sup>2</sup>The experimental results show that even for Bond numbers as high as 2.5 the influence of gravity on the tip speed is negligible

identified by two parameters, namely the Bond number and the contact angle,  $\theta$ , using the Young-Laplace equation. The contact angle of a liquid is the angle between the tube's wall and the liquid, see figure 2. Among other jet parameters, the shape, volume flow, and tip speed will depend on the focusing effect caused by the shape of the meniscus (Antkowiak *et al.*, 2007; Longuet-Higgins, 2006; Tagawa *et al.*, 2012).

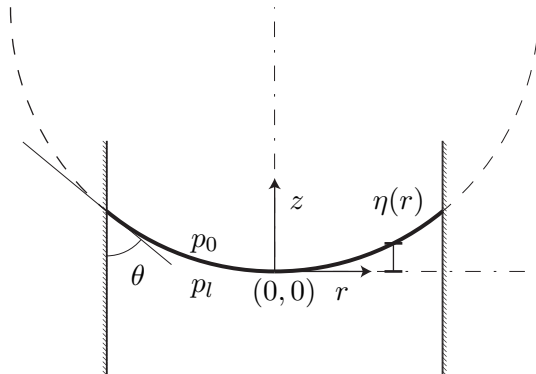


Figure 2: Schematic drawing of a meniscus (thick black curve between the two vertical lines representing the walls of the tube) with non-zero contact angle,  $\theta$ . The meniscus is drawn as a segment of a circle, which is approximately true for a low Bond number.

The pressure difference over a curved surface can be computed using the Young-Laplace equation,

$$\Delta p = p_0 - p_l = 2K\sigma = -\sigma \nabla \cdot \hat{\mathbf{n}}, \quad (6)$$

where  $\hat{\mathbf{n}}$  is the normal pointing out of the surface and  $K$  is the mean curvature.

To obtain the static meniscus shape, one needs to solve the Young-Laplace equation for generalized curvature in two dimensions, namely horizontal ( $r$ ) and vertical ( $z$ ) as shown in figure 2. The meniscus shape follows a (one-dimensional) curve in the  $rz$ -plane that is defined by the function  $z = \eta(r)$ . The origin is taken at the centre of the meniscus,  $\eta(0) = 0$ . The generalized curvature can then be written as

$$\nabla \cdot \hat{\mathbf{n}} = \frac{-\eta_r - \eta_r^3 r \eta_r}{r(1 + \eta_r^2)^{\frac{3}{2}}} \quad (0 < r < R), \quad (7)$$

where a subscripted  $r$  means the derivative to  $r$  (Zijlstra, 2007).

The pressure difference over the curved surface consists of two factors,

$$\Delta p = -\rho g \eta - 2K\sigma, \quad (8)$$

where the first factor is the hydrostatic pressure, which accounts for the height difference between  $\eta(r)$  and  $\eta(0)$ . An increase in radius leads to an increase in height. Therefore, the hydrostatic pressure decreases with  $\eta$ . Because the problem is axisymmetric, it needs to be solved only for  $0 < r < 1$ . To do so, one has to take into account the curvature at  $r = 0$ , which is the second factor. The pressure

## 2. Theory

---

difference caused by the curvature at the origin follows from the Young-Laplace equation, and equals  $2K\sigma$ . Because a curvature will lead to a lower pressure in the liquid (the outside) than at the surrounding air (the inside), one has to subtract it.

Equation 6 then results in the following differential equation

$$-\rho g\eta - 2K\sigma = \sigma \frac{-\eta_r - \eta_r^3 - r\eta_{rr}}{r(1 + \eta_r^2)^{\frac{3}{2}}} \quad (0 < r < R). \quad (9)$$

This can be non-dimensionalised using

$$\eta = \tilde{\eta}R \quad \text{and} \quad r = \tilde{r}R, \quad (10)$$

which results in

$$\frac{\tilde{\eta}_r + \tilde{\eta}_r^3 + \tilde{r}\tilde{\eta}_{rr}}{\tilde{r}(1 + \tilde{\eta}_r^2)^{\frac{3}{2}}} - Bo\tilde{\eta} - 2K = 0 \quad (0 < r < 1). \quad (11)$$

where  $Bo$  is the Bond number defined in section 2.1. The boundary condition that must be satisfied at the wall and in the centre are, in non-dimensionalised coordinates,

$$\tilde{\eta}_r = 0 \quad \text{at} \quad \tilde{r} = 0, \quad \text{and} \quad (12)$$

$$\tilde{\eta}_r = \frac{1}{\tan \theta_c} = \cot \theta_c \quad \text{at} \quad \tilde{r} = 1. \quad (13)$$

Another way of writing equation 11 is

$$\frac{1}{r} \frac{d}{dr} \left[ \frac{r\eta_r}{(1 + \eta_r^2)^{1/2}} \right] - Bo\eta - 2K = 0 \quad (0 < r < 1), \quad (14)$$

which can be represented in a parametric form by using parameter  $\Phi = \tan^{-1} \eta_r$ , the angle between the surface and the horizontal. By doing so, it can be numerically solved using an initial-value, or shooting method to solve the ordinary differential equation in multiple iterations (Concus, 1968). In that paper it is shown from a mathematical point of view that the solution converges to a spherical segment as the Bond number goes to zero. From a physical point of view, as the Bond number goes to zero, there is no influence of gravity to counter the surface tension force. Therefore the surface tension will make the surface as smooth as possible, due to surface area minimization. The smoothest area, under the boundary condition of a fixed contact angle  $\theta_c$ , is a spherical segment. A larger contact angle will thus create a spherical segment with a lower curvature, or higher radius. A meniscus is called concave or convex, when  $\theta_c < 90^\circ$  or  $\theta_c > 90^\circ$ , respectively.

### 2.2.2. Focusing effect

A focused liquid jet has a tip radius that is approximately an order of magnitude smaller than the radius of the free surface it originated from. As a result of the focusing effect, the tip speed is higher than expected from the particle velocity

(equation 25) . The focusing effect in a given tube will be maximum when a sphere with radius equal to the tube radius fits best to the meniscus, like in figure 6, because this results in the maximum curvature of the surface, within the restrictions of the Young-Laplace equation and axisymmetry. Another way of saying this is that the contact angle must be  $0^\circ$  and the Bond number must be low. That the focusing effect and thus tip speeds will be maximum then can be argued using incompressible potential flow analysis (Antkowiak *et al.*, 2007). In that particular paper a bouncing tube with fluid inside is modelled as if it is impulsively started with velocity  $U_0$ , with an impulse pressure ( $P = \int_0^t p dt$ ) at the free surface which satisfies  $P = 0$ . Under the appropriate boundary conditions, this leads to a trivial solution for the impulse pressure field  $P = -\rho V_0 z$ . Including the dynamics via  $\frac{\delta u}{\delta t} = -\frac{1}{\rho} \nabla p$  thus that each particle gets a velocity  $U_0$  in the  $z$  direction, because the gradient of the impulse pressure equals the velocity of liquid. The incompressible potential flow model then models this as if at the moment of bouncing, this pressure field is instantaneously created inside the tube. With a flat free surface, thus a contact angle of  $90^\circ$ , the particles move with the tube and in that case no jet will be created. For a curved surface, however, the velocity of some fluid particles will be enhanced due to strong inhomogeneity of the pressure gradient and inherent focusing effect (Antkowiak *et al.*, 2007). This focusing effect, for a bubble of radius  $R_b$  and height  $H$  inside a big tube, can be described by

$$\frac{\partial P}{\partial z} \sim \rho U_0 \frac{H}{R_b}, \quad (15)$$

This formula can also be used to describe a curved meniscus, instead of a bubble, where  $\frac{H}{R_c} = 1$  means a completely wetting liquid in a tube of radius  $R = R_s$ , where  $R_s$  is the radius of the sphere that fits onto the meniscus. The effect of contact angle, when neglecting gravity, can be found when  $\frac{H}{R_s}$  in formula 15 is rewritten, using geometrical arguments, to

$$U \sim U_0(1 - \sin \theta_c). \quad (16)$$

The results of this theory will be compared with the experimental results in figure 15 in section 4.

Another description of the proportionality between curvature and tip speed is given next. Because of the analysis of Antkowiak et al, two factors are important to describe the flow focusing, namely the initial velocity  $U_0$ , and the curvature  $\kappa$ . Curvature is given by  $\kappa = \frac{2}{R_s}$ , where  $R_s$  is the radius of the sphere that fits onto the meniscus. Using  $R_s = \frac{R}{\cos \theta_c}$  one can express the curvature, when neglecting gravity, as

$$\kappa = \frac{2 \cos \theta_c}{R}. \quad (17)$$

Dimensional analysis on the acceleration results in the following scaling for the acceleration

$$a \propto U_0^2 \frac{\cos \theta_c}{R}, \quad (18)$$

## 2. Theory

---

and the focusing time scale  $\Delta t$  is provided by the typical velocity  $U_0$  and length scale  $R$ :

$$\Delta t = \frac{R}{U_0} \quad (19)$$

Together they will result in a formula for the increase in velocity due to flow focusing of

$$\Delta U = a\Delta t \sim U_0 \cos \theta_c, \quad (20)$$

where  $U_0$  is the relative speed, dependent on pressure (Tagawa *et al.*, 2012). This shows that the focusing effect is diameter independent. This does not mean that the tip speed is in general indifferent to scale in all experiments, because the generation and evolution of the pressure pulse can depend on scale. This, in turn, makes the tip speed scale-dependent as will be shown in section 2.3. For the tip speed calculation one must take the velocity of the liquid without the focusing effect into account as well and therefore the formula used for comparison with experiments reads

$$U = U_0 + \Delta U = U_0(1 + \beta \cos \theta_c). \quad (21)$$

### 2.3. Effect of pressure on tip speed

Linear acoustic wave theory is used to describe the pressure pulse that travels through the liquid column (Thompson, 1971). This means that the energy of the wave is described by the acoustic energy formula,

$$E = \frac{A}{\rho c} p^2 \Delta t. \quad (22)$$

Combining the kinetic energy formula with the acoustic energy formula gives the average velocity of fluid particles under an average pressure,

$$\frac{1}{2} m U^2 \sim \frac{A}{\rho c} p^2 \Delta t \sim f(E_i) \rightarrow U^2 \sim 2 \frac{A}{\rho c m} p^2 \Delta t \quad (23)$$

where  $E_i$  is the input energy.

Using the momentum formula,

$$mU \sim pA\Delta t \rightarrow m \sim \frac{pA\Delta t}{U} \quad (24)$$

to substitute the mass ( $m$ ) in equation 23, this leads to the particle velocity in a liquid bulk ( $U_b$ ),

$$U_b \sim \frac{p}{\rho c}. \quad (25)$$

For a closed system would hold  $p \sim \frac{1}{\text{sqrt}(A)}$ , this follows from conservation of energy and using equation 22. Thus a decrease in the areal cross-section of the liquid column increases its pressure if the input energy, and thus the energy of the pressure wave stays the same. The system described in this thesis is not closed, because

the glass tube, with area  $A_g$ , is submerged in the steel tube (area  $A_s$ ) and is not sealed. However, the energy per area, and thus the average pressure in the steel tube and the capillary glass tube is the same, because part of the pressure wave continues undisturbed. Therefore the particle velocity in glass tube will equal the particle velocity in the steel tube. When calculating the energy efficiency of the jet formation process it should be taken into account that a part of the energy does not contribute to the jet formation, namely  $E_{loss}$ , equal to

$$E_{loss} \sim \frac{A_s - A_g}{\rho c} p^2 \Delta t, \quad (26)$$

because part of the pulse is continued outside the glass tube and does not contribute to the jet formation.

Equation 25 gives the velocity of the fluid particles under influence of the pressure pulse in the liquid column or liquid bulk. To get the tip speed of the jet the interaction with the free surface has to be considered. In general, the reflection at a surface is characterised by the composition of the media which form the interface, and then especially by their acoustical impedances. The acoustical impedance, is defined as

$$Z = \rho_0 c_0 \quad (27)$$

and is of a completely different order in water than in air, respectively  $1.5 \times 10^6 \text{ kg/m}^2 \text{ s}$  and  $4.1 \times 10^2 \text{ kg/m}^2 \text{ s}$ . This acoustical mismatch results in 99% reflection of the pressure pulse at the free interface, and a surface velocity  $U_s$  which is about twice the particle velocity in the bulk, according to

$$U_s = \frac{2Z_{water}}{Z_{water} + Z_{air}} U_b \sim 2U_b. \quad (28)$$

This analytical expression for the free surface velocity  $U$ , is derived by considering a 1-dimensional plane step function wave under the acoustic approximation (Thompson, 1971). Others have also derived the factor 2 due to the reflection of the pressure wave, for example by a theoretical derivation (Kedrinskii & Translated by Svetlana Yu. Knyazeva, 2005; Cole, 1948).

To acquire the jet speed, the reflection at the free surface and focusing effect will be included in equation 25, which results in

$$v_{tip} \sim 2C_{foc} \frac{\Delta P}{\rho c}, \quad (29)$$

where  $C_{foc}$  is the focusing effect due to the shape of the meniscus, which depends on the contact angle. Research for zero contact angle and small Bond number showed that for 2-dimensional simulation, this focusing factor is around 1.5 (Mader, 1965). In three dimensions this focusing effect is logically bigger, previous research has found this factor to lie around 2.5 for zero contact angle (Zijlstra, 2007). For  $C_{foc}$  also a contact angle dependent factor derived in section 2.2 can be used.

## 2. Theory

---

### 2.4. Jet Breakup

Jets are inherently unstable, they will break up into droplets to minimize its surface energy (de Gennes *et al.*, 2004). The jets described in this report have a high Weber number, therefore the droplet formation can be characterised as ‘Rayleigh breakup’ (Rayleigh, 1879; Plateau, 1873; van Hoeve *et al.*, 2010). Because jets are unstable, first they develop into a wavy profile after which they breakup into droplets. The fastest growing perturbation has a wavelength of

$$\lambda_{opt} = 2\sqrt{2}\pi r_{jet}, \quad (30)$$

and a characteristic time determined by the equilibrium between the inertia term ( $\frac{\rho r_{jet}}{\tau^2}$ ) and the capillary term ( $\frac{\sigma}{r_{jet}^2}$ ). This leads to a time scale of

$$\tau_c \approx \sqrt{\frac{\rho l r_{jet}^3}{\sigma}}, \quad (31)$$

which is called the capillary time. A liquid jet will thus breakup into droplets in a time of order  $\tau_c$ . The resulting volume of the droplets is given by

$$Vol = \lambda_{opt}\pi r_{jet}^2 = 2\sqrt{2}\pi^2 r_{jet}^3 \sim 4/3\pi r_{droplet}^3, \quad (32)$$

where  $r_{droplet} \approx 1.88r_{jet}$  is the characteristic droplet size. (de Gennes *et al.*, 2004). This means that the final characteristic droplet size depends on the radius of the jet only.

The derivation of the above-mentioned equations uses the lubrication approximation ( $z \gg r$ ), thereby simplifying the Navier-Stokes equation (Rayleigh, 1879; Plateau, 1873; de Gennes *et al.*, 2004). To model the jet breakup in more detail, numerical simulations can be used which shown the time evolution of the jet when it breaks up (van Hoeve *et al.*, 2010).

### 2.5. Potential flow and boundary integral theory

Axisymmetric Boundary Integral (BI) simulations have been performed by Peters for the experimental setting in this thesis (Peters, 2011). The simulations are based on potential theory, like for example the analysis of (Antkowiak *et al.*, 2007). Potential flow assumes an incompressible fluid, thus a pressure pulse applied at a wall creates instantaneously a pressure field inside the whole domain. Because the Reynolds number is high in the experiment described in this thesis, viscous forces can be neglected. This means that the potential flow analysis is applicable to model the experiment. Because the fluid is treated as incompressible, a bubble is placed in the liquid column to provide for the liquid that goes out with the jet. In fact, Laplace’s equation is solved,

$$\nabla^2\varphi = 0, \quad (33)$$

where  $\varphi$  is the velocity potential. The BI method solves the Laplace equation for one-dimensional curved boundaries, by using Green’s identity and evaluating an

area integral across the boundary to calculate the resulting jet formation (Oguz & Prosperetti, 1993). In this simulations, an approximation of the measured pressure signal is applied as input (Peters, 2011).

## 3. Experimental setup

*This chapter describes the methods that create and measure the pressure pulse and jet formation. In short, reproducible pressure pulses are created using an eddy-current actuator. The pressure is measured with PVDF pressure sensors, flush mounted at the wall of the steel tube. High-speed imaging devices visualize the jet formation for contact angles ranging from 0° to 90°.*

### 3.1. The shocktube experiment

The shocktube experiment in this study used a vertically aligned steel tube fitted with an eddy-current actuator at its bottom and an immersed capillary tube of varying diameter at its top (see figure 3): a flat pressure pulse, created at the bottom of the liquid column, propagated to the free surface in the capillary tube, where the subsequent jet formation and jet evolution were studied using a high-speed imaging device (Photron SA 1.1 or Photron SA 2, Photron company, Buckinghamshire, UK). The pressure of the pulse was measured with flush-mounted PVDF pressure sensors at the wall and a data acquisition system (PXI by National Instruments, Texas, US). The steel tube was filled with ultrapure water from a Milli-Q device (by Millipore Corporation, Massachusetts, US). The water was degassed by decreasing the pressure in a filtering flask to less than 120 mbar and gently rotating a magnetic stirrer for an hour.

### 3.2. Eddy current actuator

An eddy current actuator was used to create pressure pulses. The eddy current actuator consists of a multi-layered coil with a copper plate on top. The copper plate is held in place by two foils, where the upper foil forms a watertight connection with the rest of the steel tube. The eddy current actuator was driven by a high voltage capacitor bank, which was charged to a voltage  $U_C$ . Triggering a high-voltage transistor by an external function generator resulted in the discharge of the stored energy on the coil that generated a pulsed magnetic field. Figure 4 shows the relation between  $U_C$ , the input energy,  $E_{el}$ , and the resulting maximum and mean pressure that was measured using the PVDF pressure transducers at the wall of the steel tube. The relation between input energy and resulting pressure amplitude is shown to be linear. The input energy is defined as

$$E_{el} = \frac{1}{2}CU_C^2. \quad (34)$$

The current gives rise to a magnetic field, equal to

$$\oint \mathbf{B} \cdot d\mathbf{l} = \mu_0 nI, \quad (35)$$

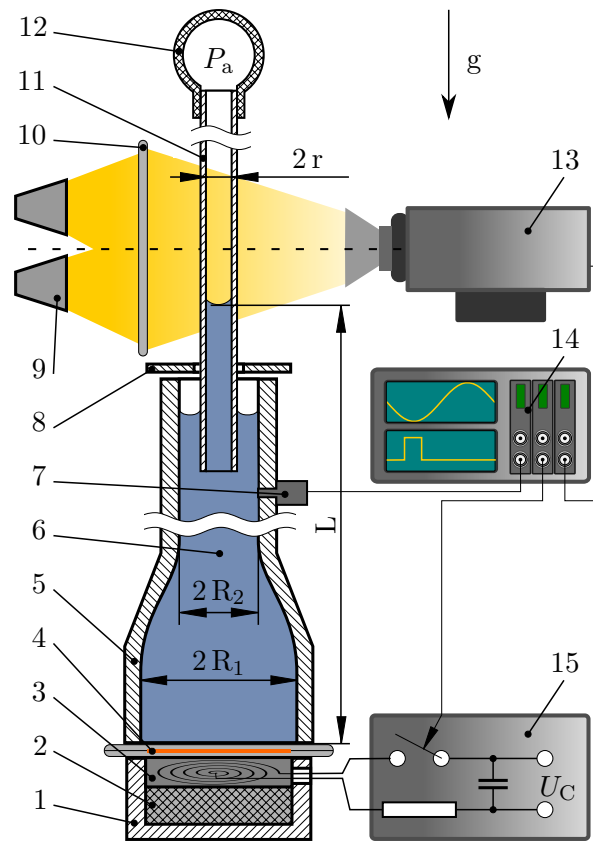


Figure 3: Schematic diagram of the experimental setup: (1) Support of the coil made of stainless steel, (2) Non-magnetic spacer between coil and support made of pertinax, (3) Flat spiral multilayer copper coil embedded in cyanoacrylate, (4) Copper disc between two supporting foils, (5) Cylindrical tube made of stainless steel (diameters of  $2R_1 = 44$  mm and  $2R_2 = 25$  mm, minimum wall thickness of 8 mm), (6) Ultrapure water from a Milli-Q device (Milli-Q Advantage A10 by Millipore Corporation, Massachusetts, US) (7) PVDF pressure transducer (M60-1L-M3 by Müller Instruments(Oberursel, Germany), rise time of 50 ns) and fiber optic probe hydrophone (FOPH 2000 by RP acoustics e.K. (Leutenbach, Germany)), (8) Splash guard (tissue), (9) Halogen light source (Mega Beam Xenon by Hella KGaA Hueck & Co. (Lippstadt, Germany)), (10) Milk-white diffusive plate, (11) Cylindrical capillary tube made of Schott-Duran® glass (DURAN Group GmbH., Wertheim, Germany) (diameter of  $2R = 4$  mm to 8 mm, distance between free surface and copper disc of  $L \approx 1.1$  m), (12) Hand pump, (13) High speed camera (Fastcam SA 1.1 by Photron Limited) equipped with macro lens (Makro-Planar T\* f/2.8 60 mm by Carl Zeiss AG (Jena, Germany)), (14) Data acquisition system (PXI-5124 by National Instruments (Texas, US), bandwidth of 145 MHz) and function generator (AFG3000 Series by Tektronix, Inc. (Oregon, US)), (15) High voltage capacitor charging device (HCK 100-3500 by FuG Elektronik GmbH (Rosenheim, Germany), voltage of  $U_C = 0$  V to 3500 V) and capacitor bank (capacity of  $C = 80/3 \mu\text{F}$ ).

### 3. Experimental setup

---

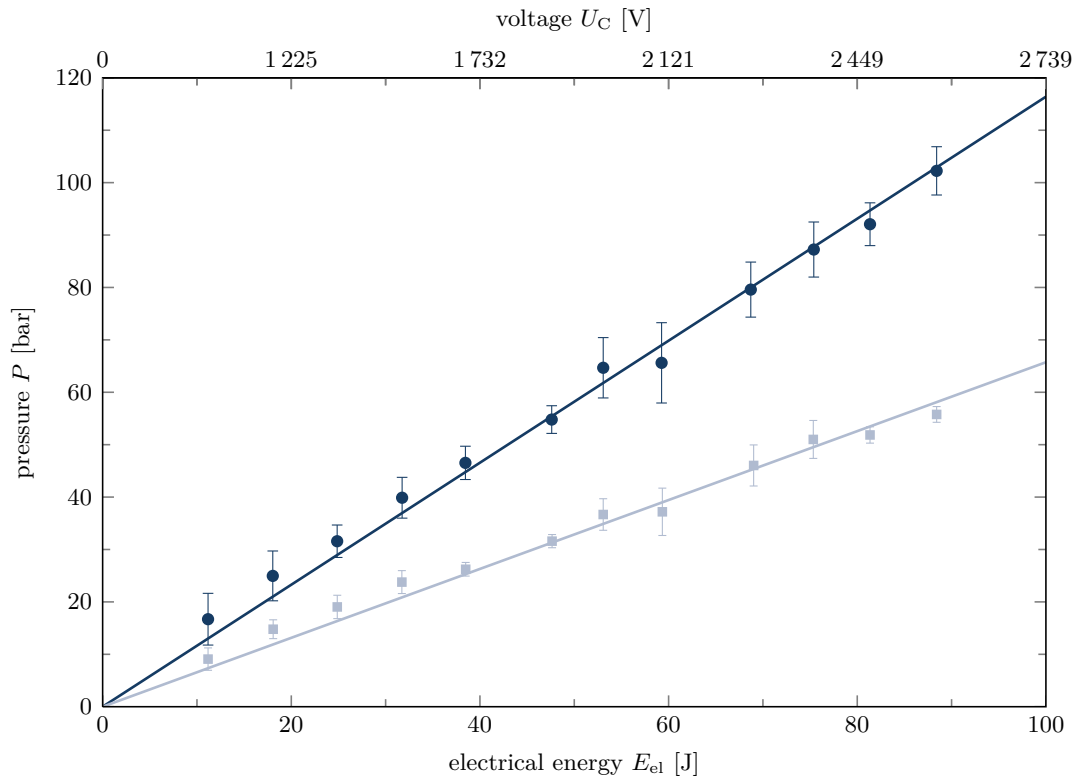


Figure 4: Experimental relation between electrical energy input  $E_{el}$ , voltage  $U_C$  and maximum pressure  $P_{max}$  ( $\bullet$ ) as well as mean pressure  $\bar{P}$  ( $\blacksquare$ ) for the utilised eddy-current actuator. A linear relation is observed:  $P_{max} = 1.164 \text{ bar/J } E_{el}$  (—) and  $\bar{P} = 0.6573 \text{ bar/J } E_{el}$  (—). The illustration is based on 780 single experiments and the error bars indicate the sample standard deviation for each data point.

where  $n$  is the number of windings. This means a (high) flux through the copper plate, as follows from

$$\Phi_b = \iint_S \mathbf{B} \cdot d\mathbf{S}. \quad (36)$$

This will induce an electromotive force in the copper plate which, according to Lenz's law, will oppose the flux of the coil,

$$\epsilon = -\frac{d\Phi_B}{dt}, \quad (37)$$

where  $\epsilon$  is the electromotive force. Since opposing magnetic fields have a repulsive nature, the copper plate will shoot up. The time it takes to unload the capacitor is very small, which means that the induced magnetic field and thus the repulsive force will be big. To prevent damage of the support of the tube and of the foil, a non-conducting spacer of pertinax was placed between the coil and support. The thickness of the wires has an influence on the strength of the shooting force of the copper plate. Table 2 demonstrates that, a thinner wire will give you more windings for a given tube diameter, but a bigger wire has less resistance and thus a higher current. To compare the usability of different coils a relative magnetic field strength is introduced:

$$B_r = n/\mathcal{R}, \quad (38)$$

where the number of windings ( $n$ ) can be estimated by taking the tube diameter (approximately 21.5 mm in the experiment in this thesis) and divide it by the thickness of the wire and then multiply it by the number of layers (4). Practically, the wires can be packed slightly closer together, because of the elasticity of the outer layer of the wire.

| Wire type | Resistance ( $\mathcal{R}$ )<br>[ $\Omega$ ] | Outer Diameter<br>[mm] | Number of windings ( $n$ )<br>[-] | Relative magnetic field strength ( $B_r$ )<br>[ $T\Omega^{-1}$ ] |
|-----------|--|------------------------|-----------------------------------|--|
| 20AWG     | 1.1  | 1.09                   | 78                                | 87.5   |
| 22AWG     | 0.8  | 1.29                   | 70                                | 70.91  |

Table 2: Wire characteristics and the resulting relative magnetic field strength in the coil.

This pressure pulse formation mechanism has several advantages over explosion and bullet-piston methods: firstly, this mechanism creates reproducible pressure pulses. Secondly, the waiting time between shots is low, and thirdly, the time-lag between the trigger and the actual shot is very small and consistent between shots.

### 3.3. Pressure sensors

Two types of pressure sensors, based on different physical phenomena, are compared in this section. The first is a pressure sensor based on the change of reflectivity when the density of the liquid changes, the other is a pressure sensor based on

### 3. Experimental setup

---

the piezo-electric effect. For all pressure measurements that are used in this thesis the PVDF pressure sensor was used. However, to show that the rise-time of the PVDF pressure transducers is high enough, a comparison with the Fiber Optic Probe Hydrophone (FOPH) has been made.

#### 3.3.1. Fiber Optic Probe Hydrophone (FOPH)

The Fiber Optic Probe Hydrophone (FOPH) is based on the physical principle that the reflectivity of a liquid/glass interface changes locally when the pressure changes. Due to the small tip of the fiber, it enables a very local measurement of the pressure. To see why the reflectivity of the interface changes, one has to look closely at a pressure pulse in liquid. If the pressure becomes higher this will lead to a higher density in the gas or liquids, because it compresses the liquid or gasses. To find how exactly the density changes when a pressure pulse comes by, equations of state are used, which are based on experimental data in the positive pressure regime. If the density changes, also the refractive index changes. According to the Fresnel equations, this leads to a change in reflectivity. By measuring the intensity difference between the send and received laser pulse, a way of measuring with high spatial and (depending on the way the signal is handled) temporal resolution is obtained. In practise a lot of noise is present in FOPH measurements, because of cavitation and brown noise of the laser, and an average over at least 50 shots is needed to get a well-defined signal (Zijlstra & Ohl, 2008). Because a change in density is measured, also a change in temperature will affect the measurement. For measuring negative pressures, the uncertainty of the current types of equations of state, which are calibrated in the positive pressure region, becomes bigger. This means that the more negative the pressure becomes, the bigger the deviation will be between the measured pressure and the real pressure. Cavitation at the fiber tip can destroy the tip, whereas a sticking bubble at the tip can drastically influence the measurements. A new tip can be made by cutting the fiber, however after this cutting calibration is essential to test the new tip. The sensor used for comparison (FOPH2000) exhibits a rise time of 3 ns and a sensitive diameter of 100  $\mu\text{m}$  is made by RP acoustics e.K. (Leutenbach, Germany).

#### 3.3.2. PVDF piezoelectric pressure sensors

Piezoelectricity is a reversible effect in which an internal charge is generated when a mechanical force is applied. Since a direct relation exists between the amount of pressure and the internal charge, a sensor based on this effect can be used to measure the pressure pulse. Polyvinylidene fluoride is a material that was observed in 1969 to exhibit strong piezoelectric characteristics (Kawai, 1969). PVDF's piezoelectric coefficient is as large as 6  $\text{pC N}^{-1}$  to 7  $\text{pC N}^{-1}$  (about ten times bigger than other polymers). Another characteristic of PVDF is that it compresses and not expands (or vice versa) when exposed to the same electric field, compared to most common piezoelectric devices. This means that when a positive voltage is measured, a negative

pressure is actually measured. Because temporal and spacial resolutions of sensors based on the piezoelectric effect has increased substantially, and because of its ease of use, this sensor is ideal for the type of measurements done in this thesis. However, the manufacturer indicated that its function is not known exactly for negative pressures below 20 bar. The sensor used in this thesis (M60-1L-M3, Müller Instruments, Oberursel, Germany) exhibits a rise time of 50 ns and has a sensitive diameter of 1 mm. The sample rate was 20 MHz and the pressure records were acquired over 20 ms. For plotting purpose the data was digitally filtered with a Chebyshev type II filter at a cut-off frequency of 2 MHz.

#### 3.3.3. Comparison of FOPH and PDVDF pressure sensors

Figure 5a shows a comparison of the PVDF and the FOPH on a normalized pressure scale for a single shot. At the very first instant ( $t < 15 \mu\text{s}$ ) the PVDF pressure record shows a high frequency noise that was caused by the electromagnetic field during the discharge of the capacitor bank, whereas the FOPH was galvanically isolated and did not show this effect. The FOPH exhibits large variations in the signal amplitude when used for measuring pressure pulses without shot averaging, especially in a cavitation liquid (Zijlstra & Ohl, 2008). Spatial pressure fluctuation are more likely to be resolved by the FOPH as compared to the PVDF due to the smaller sensitive diameter of 100  $\mu\text{m}$  compared to 1 mm. This explains the difference in absolute pressure amplitude of 25 % for the given pressure record in figure 5a. In the negative pressure region local cavitation events can disturb the signal as shown in figure 5a for the FOPH (—). Both signals exhibit the same features and compare very well in the positive pressure region. The comparison verifies the applicability of the PVDF transducer in the experimental setup used in this study. Figure 5b illustrates the order of magnitude of the deviation in pressure among several shots: the experimental setup allows for generating single pressure pulses in a reproducible way at amplitudes of the order of 100 bar and with a rise time and duration of about 30  $\mu\text{s}$  and 100  $\mu\text{s}$ , respectively. Assuming a flat spatial pressure pulse and an undisturbed propagation the pressure amplitude at the free surface inside the capillary tube correlates with the recorded pressure signal of the PVDF transducers.

### 3.4. Glass tubes

#### 3.4.1. General tubes

Cylindrical capillary tubes made of Schott-Duran® glass (DURAN Group GmbH., Wertheim, Germany) were used in this thesis. These were cut to a length of 75 cm and hung in the steel tube using clamps on the outside. The wall thickness ranged from  $(1.0 \pm 0.1)$  mm to  $(2.0 \pm 0.2)$  mm and the inner diameter ranged from 4 mm to 8 mm. Two sealing tubes were made, one with a diameter of 8 mm and the other with a diameter of 24 mm, to be used with a flanche. The sealed tubes were not used in obtaining the results, because these resulted in an unknown amplitude of

### 3. Experimental setup

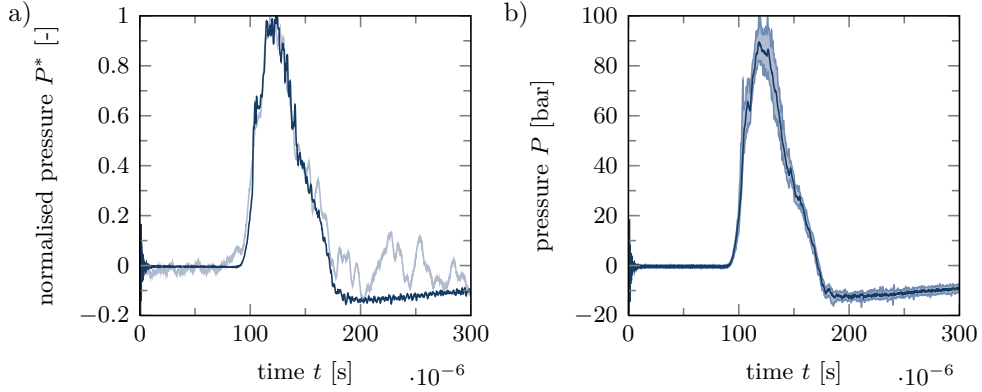


Figure 5: a) Comparison of a single pressure record acquired simultaneously by a FOPH (—) and a PVDF pressure transducer (—). The time  $t = 0$  corresponds to the discharge of the capacitor bank on the coil. The distance of the measuring point to the copper disc at the tube’s bottom is 0.125 m leading to a delay of the initial pressure rise of 80  $\mu$ s. b) Mean pressure record (—) based on 100 single shots at a constant voltage of  $U_C = 2200$  V and acquired by a PVDF pressure transducer. The shaded area (■) indicates the maximum deviation from the mean record for each sample in time.

the pressure pulse at the free surface. Hydrophobically coated and uncoated glass tubes were used for the experiment. Uncoated tubes were cleaned before by using Kimtech® (Kimberly-Clark Professional B.V., Ede, Netherlands) dust-free tissue wetted by ethanol and then acetone. After cleaning, the inside and outside of the tube were rinsed with demi water to remove all ethanol and acetone.

#### 3.4.2. Coated tubes

Before coating the capillary tubes, they were cleaned using a piranha solution (30% (volume-percent) hydrogen peroxide (30%) with 70% sulfuric acid (95-98%)). Capillary tubes were kept in a tube-shaped beaker and were fully covered with the piranha solution. The tubes with the piranha solution are kept under the fume hood for 20 hours. Later, atomic force microscope studies pointed out that cleaning with ethanol and blowing dry using nitrogen turns out to be a more safe and effective cleaning procedure, see appendix A.4. The next step was coating the tubes using 5% (volume-percent) 1H,1H,2H,2H-Perfluorooctyltrichlorosilane 97% dissolved in 95% cyclohexane. The solution was poured into the capillary tube, while sealing the lower end of the tube, until the tube was half full. The tube is then put at rest for 1 hour in the flow-cabin. It is observed that when taking them out after an hour, the liquid level had sunk several cm. This accounts very likely for the observed transient in wettability. The transition region enabled the formation of several meniscus shapes with different contact angles. To make these meniscus shapes the hydrophobic coated side of the tube had to be on top, and a handpump was used to rise or lower the free surface.

## 4. Experimental results and Discussion

*In this chapter the experimental results are displayed. First, some general results for processing the jets, such as tip speed, volume flow, and flow speed over time are presented (section 4.1). Next, the effect of the pulse pressure on tip speed are reported (section 4.2). Then, section (4.3) presents the effect of contact angle on jet speed. In the last section results for the relations between tip speed and tube radius are shown (4.4).*

### 4.1. General results

Figure 6 shows an image sequence of a typical experiment conducted in this thesis. The visualized section of the tube and fluid are completely at rest at time  $t_1$ . At time  $t_2$  the pressure pulse is already reflected from the free surface leading to an acceleration of the meniscus. The passing of the pressure pulse is indicated by the presence of cavitation bubbles below the free surface. The distance of the cavitation bubbles below the free surface depends on the geometry of the experiment; the severity of cavitation depends on the pressure amplitude. The formation of a cavitation layer is also known for light underwater explosions just below a free surface (Kedrinskii & Translated by Svetlana Yu. Knyazeva, 2005). Starting at time  $t_3$ , a liquid jet is generated which evolves over time. The volume of the droplet that detaches shortly after time  $t_{12}$  is approximately  $0.2 \mu\text{L}$ .

The data acquired from the high-speed camera is analysed using MATLAB (2008). The code to process the data was made available to me by A. Klein. Each image sequence is post processed in several subsequent steps. Firstly, the jet perimeter is detected in each image by a background subtraction technique. Secondly, the refraction due to the curved surface of the tube is corrected by means of a three dimensional ray tracer. Assuming an axially symmetric jet generation and evolution the perimeter of the jet is supposed to be captured by the camera on the tube's vertical mid-plane. Therefore, the real world coordinates of each pixel on the perimeter can be determined unambiguously from a single image. Thirdly, the chord-length parametrisation of the jet is obtained and described by bivariate splines, which are used to compute jet properties, such as tip speed and volume flow. The volume flow is based on a certain height, for which the change in volume above this height is calculated. The volume is calculated from the 2D representation by using a rotation about the axis. The axis is the middle of the jet, and its coordinates vary with height. For the purpose of illustration and for comparison with simulations an axisymmetric chord-length parametrisation is computed, which is shown in figure 7 for a single experiment. Furthermore, the initial meniscus shape is determined to compute the initial contact angle and curvature. The Young-Laplace equation in its axisymmetric formulation is solved numerically and fitted to the experimental meniscus shape (Concus, 1968). The method of solving used is the shooting method. By doing this, the contact angle at the tube wall can be computed although that region is underexposed in the high speed images due to refraction. Especially in

## 4. Experimental results and Discussion

the case of the meniscus shape, the ray tracer is of great importance to correct deformations in the images due to refraction.

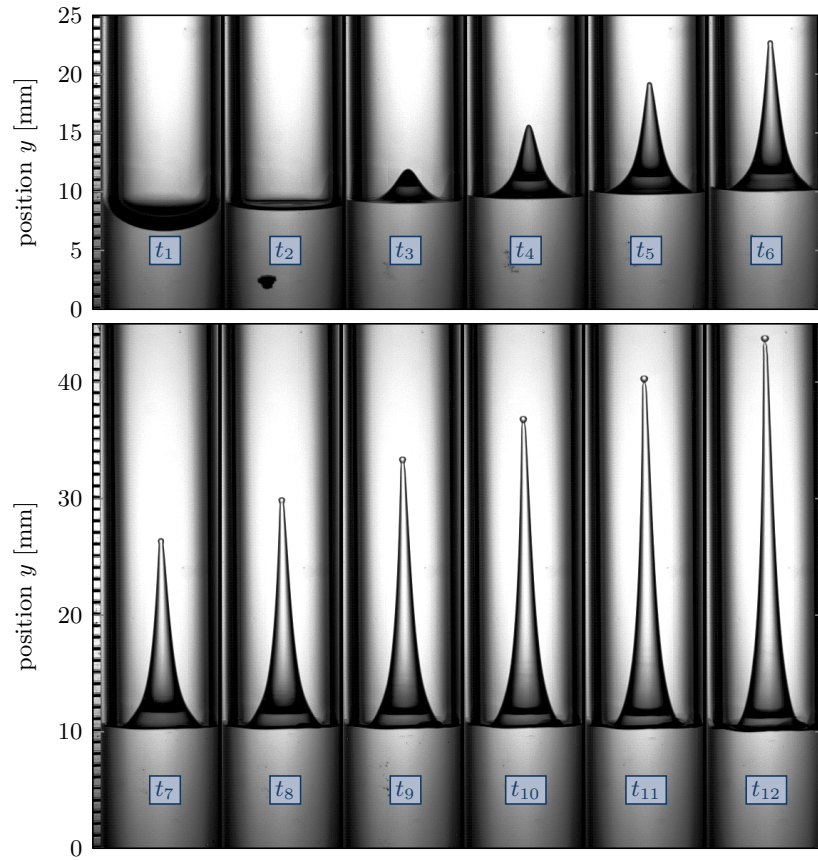


Figure 6: Image sequence as recorded by a high-speed camera at a framerate of  $16 \times 10^3$  FPS for an experiment with  $U_C = 1800$  V and  $d = 8$  mm (both representations are true to scale). The time interval separating each frame is  $\Delta t = 0.1875$  ms; the pressure pulse hits the free surface just after time  $t_1$ . Figure 10, 8 and 9 include the pressure record, jet speed, and volume flow at the positions  $y_i$  of the corresponding experiment. The point in time of each frame is indicated in those figures for better comparison.

The jet reaches its maximum speed within 0.3 ms as illustrated in figure 8 for the tip and meniscus speed. It slows down to a plateau value at a speed less than 5% lower than the top speed. The plateau speed is reached within 1 ms. The camera view is limited to capture the jet at its initial stage with a total height of several cm, whereas the jet can elongate up to several meters before it breaks up into droplets and falls down under the influence of gravity. For jet tips moving faster than  $\sim 5 \text{ m s}^{-1}$ , the role of gravity can be neglected, because the tip of the jet moves out of view before they are slowed down significantly. Equation 31 shows a relation between  $r_{jet}$  and the characteristic break-up time. Because  $r_{jet}$  decreases

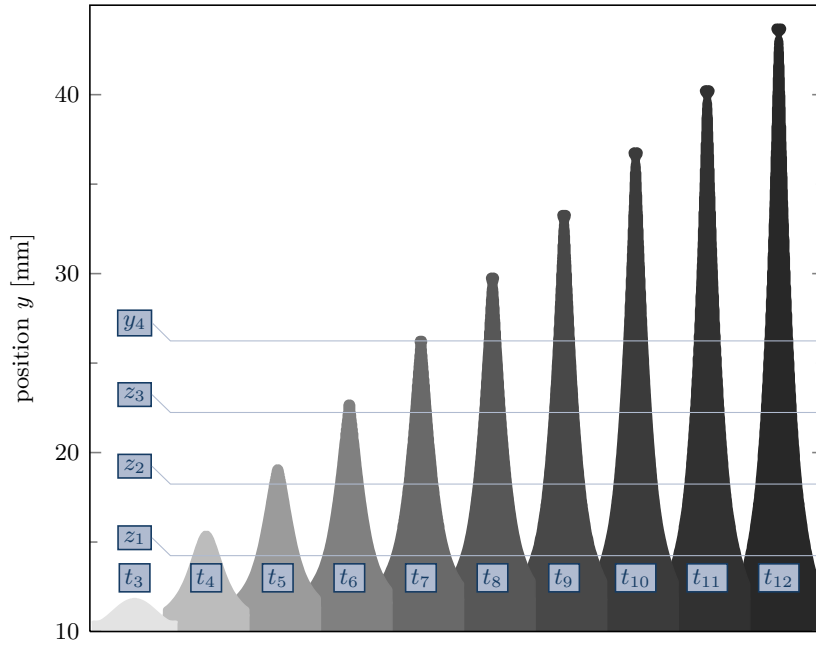


Figure 7: Digitally processed image sequence of figure 6. Note that these shapes contain the refraction correction and are obtained from the chord-length parametrisation of the jet.

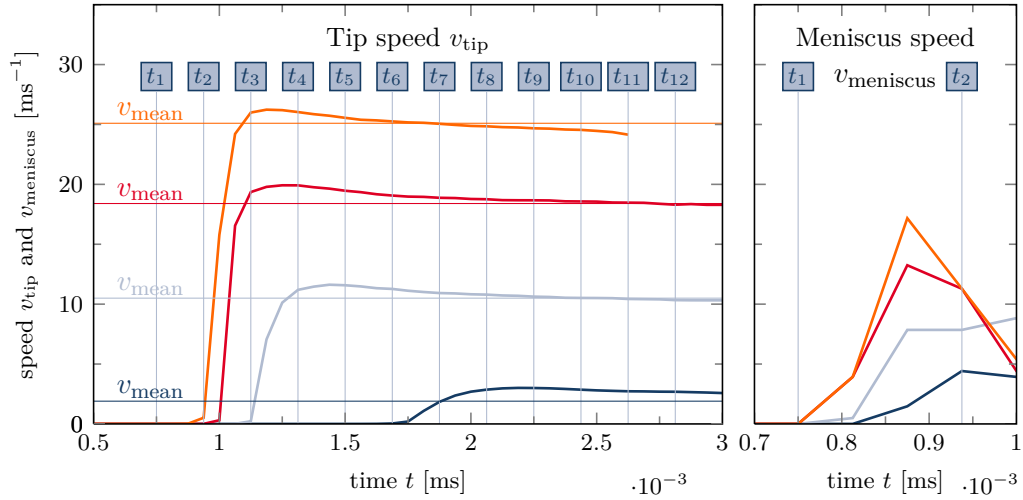


Figure 8: Speed of the jet tip,  $v_{\text{tip}}$ , and lowest meniscus point at the very beginning of the jet formation,  $v_{\text{meniscus}}$ , plotted against time  $t$  for four input voltages ( $U_C = 1200$  V —,  $1500$  V —,  $1800$  V —, and  $2100$  V —). Use figure 6 to compare with the high speed images for the experiment with  $U_C = 1800$  V (—). The delay in tip speed for the experiment with  $U_C = 1200$  V (—) is due to the fact that the tip speed cannot be detected, because the jet is still inside the meniscus region.

## 4. Experimental results and Discussion

with height, it is expected that the tip of the jet breaks up earlier than the bottom of the jet. For comparison: At 1R below the lowest meniscus point at times  $t_6$  and later,  $\tau_c \approx 4$  ms, while at the jet tip,  $\tau_c \approx 1$  ms.

Figure 9 shows a representative graph of the volume flow,  $\dot{V}$ , and flow speed,  $v_{\text{flow}}$ , for a jet at cross sections taken at different positions,  $z_i$ , shown in figure 6. The volume flow at the base of the jet (—,  $z_1$ ) rises over a longer period of time compared to the tip speed, and it reaches its maximum within 0.8 ms. Subsequently, it declines at the jet's base rapidly. Therefore, the jet grows in height due to elongation, which is verified by the flow speed at different cross sections as shown in figure 9. At constant time  $t$  the flow speed increases with position  $z$ . This means that the highest flow speed is at the tip.

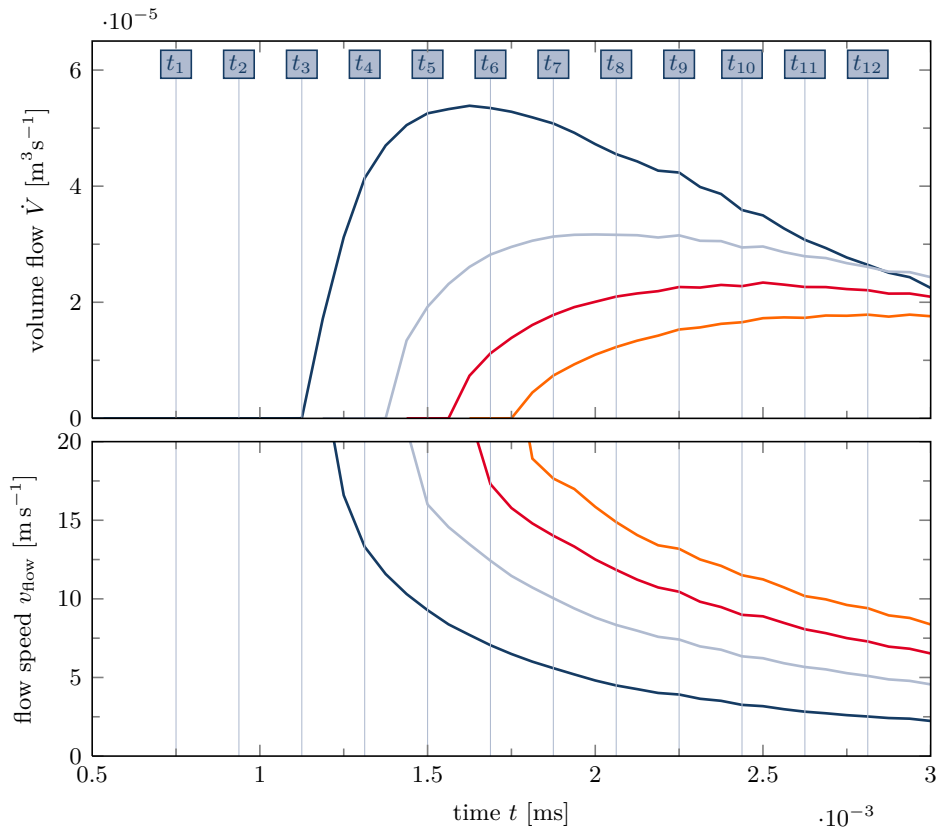


Figure 9: Volume flow,  $\dot{V}$ , and flow speed,  $v_{\text{flow}}$ , at different positions  $z_i$  along the jet plotted against time  $t$  for the jet evolution shown in figure 6: —,  $z_1$ ; —,  $z_2$ ; —,  $z_3$ ; —,  $z_4$ . Compare figure 6 for the high speed images at time  $t_i$  and the positions  $z_i$ .

## 4.2. Effect of pressure pulse amplitude on tip speed

The pressure pulse created by the eddy-current actuator travels upwards to the free surface. Figure 10 shows a record with two pressure sensors for a typical experiment. It can clearly be seen that the pressure pulse moves up, and thereby first hits the lower pressure transducer (—) and then the higher transducer (—). The estimated velocity of the pressure pulse is  $1450 \text{ m s}^{-1}$ . Before time  $t_2$ , the pressure pulse has hit the surface. No reflection of the pressure pulse is detected, a possible reason for this is elaborated in appendix (A.2.4). In short, two reasons can be given for this, firstly the pressure pulse gets reflected again when moving from the small glass tube to the big steel tube and does not pass the measured area again; secondly, the pressure pulse does not expand to the full area of the steel tube and therefore does not touch the sensor which is placed on the tube's wall. The second explanation is not very likely, because of reasons explained in the appendix (see figure 22). At a time between  $t_3$  and  $t_4$ , the lowest pressure sensor detects a high peak in the pressure, which is probably caused by the collapse of a vapour bubble close to the transducer.

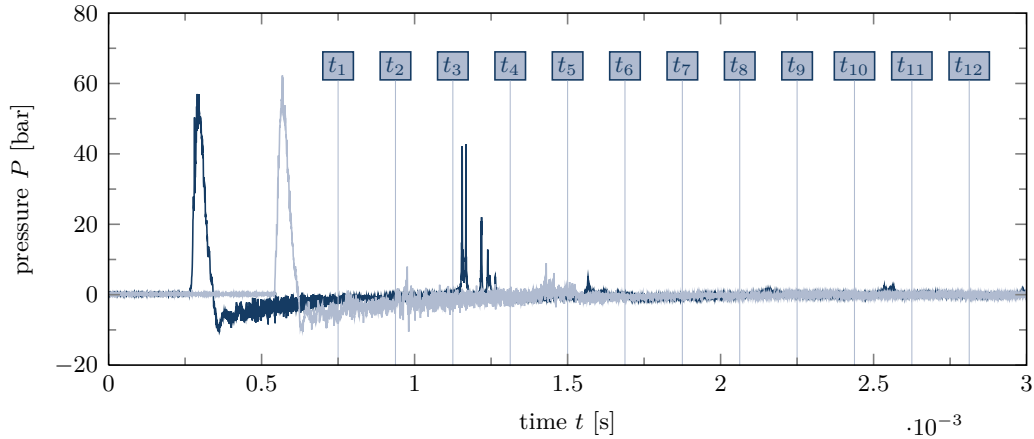


Figure 10: Simultaneous pressure record of two PVDF pressure transducers at different positions during the jet formation shown in figure 6. The distance of the transducer to the copper disc at the tube's bottom is  $0.375 \text{ m}$  for transducer 1 (—) and  $0.775 \text{ m}$  for transducer 2 (---). The propagation speed of the initial pressure pulse based on the time delay of both signals is estimated to be  $1450 \text{ m s}^{-1}$ . This leads to a propagation delay of the pressure pulse from the measuring point to the free surface of  $\sim 0.6 \text{ ms}$  and  $\sim 0.3 \text{ ms}$  for transducer 1 and 2, respectively.

As shown in figure 4 the maximum and mean amplitude of the pressure pulse are proportional to the electrical energy. Therefore  $f(E_i)$  in equation 23, can be written as

$$p^2 \sim f(E_i) \sim E_i^2 \rightarrow p \sim E_i. \quad (39)$$

In figure 11 the tip speeds is plotted over pressure and electrical energy for two

## 4. Experimental results and Discussion

different contact angles, namely  $0^\circ$  and  $60^\circ$ . For a higher curvature, a higher pressure is needed to generate a jet, which follows from the slightly higher offset. However, when this barrier is overcome, the focusing effect will increase the mean tip speed compared to a jet which is formed at a less curved meniscus. Also Oudalov (2011) found a linear relation between  $E_i$  and the tip speed, with experiments using a laser-induced vapour bubble to generate a jet. Other important parameters that affect the tip speed of the jet in his research, such as tube diameter, distance from the meniscus, and focus offset all influence the amplitude of the pressure that hits the free surface. Therefore it is important to study the effect that is responsible for the jet creation, namely the shock wave or pressure pulse in great detail to improve the understanding of the jet formation. Another remarkable observation is that, independent from the pressure generation mechanism, the (mean) pressure amplitude scales linearly with the input energy. The energy of the pressure pulse scales with the pressure amplitude squared.

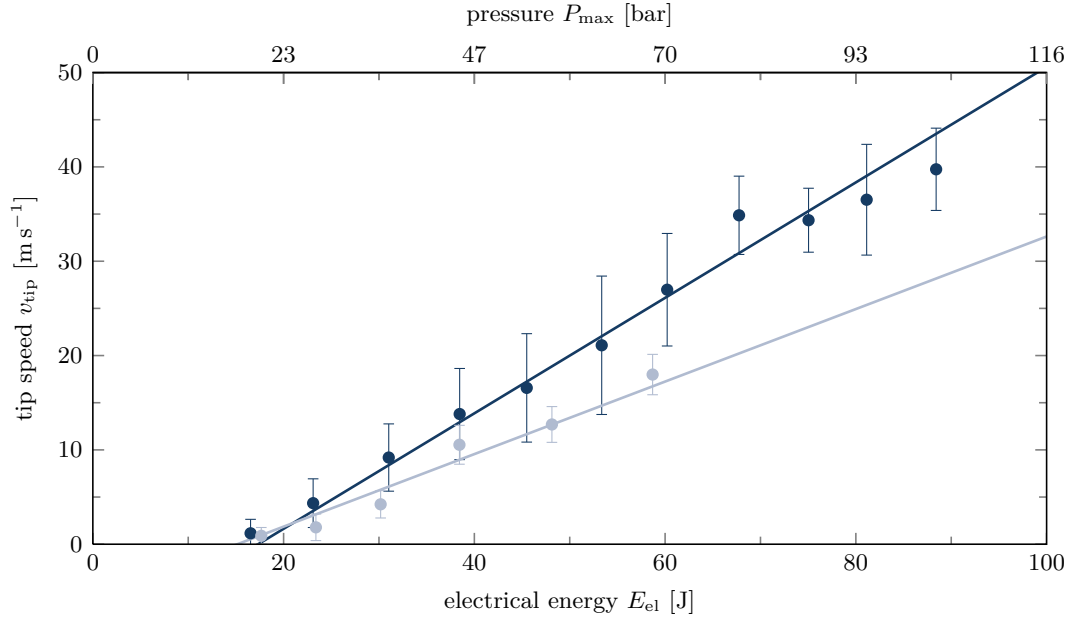


Figure 11: Tip speed over maximum pressure and electrical energy for two constant contact angles according to the experiment from this thesis and according to theory. Experimental curves are shown for  $\theta_c^1 = 0^\circ$  (●) and  $\theta_c^2 = 60^\circ$  (●), which are based on 240 and 180 single experiments, respectively. The theoretical curves (— and —) are given by  $v_{\text{tip}} = 2(P_{\text{max}} - P_0^i)/(\rho c)(1 + \beta_i \cos \theta_c)$ , where  $P_0^i$  is fitted to each experimental data set to account for an offset and  $(\rho c)$  is the acoustic impedance of the liquid. The offset ( $P_0^1 = 20.17$  bar and  $P_0^2 = 17.64$  bar) accounts for the fact, that a minimum pressure is required to generate a jet. The fitting constant  $\beta = 2.9$ , which is the value derived from figure 15 with many different contact angles.

### 4.3. Effect of contact angle on tip speed

Figure 12 shows an image sequence of a typical experiment with a partly coated glass tube filled with ultra-pure water. Because a transition region exists between the coated and the uncoated part of the tube, theoretically any contact angle between uncoated and coated can be made. This will be discussed in more detail in section 3.4.2. The image sequence shown in figure 12 is acquired by moving the meniscus to a height close to the uncoated area, so that the effect of the coating is less pronounced. As can be seen in the first image, the contact angle is small, but not  $0^\circ$  as in figure 6. The radius of the tube is 4 mm ( $Bo = 2.15$ ), which means that the influence of gravity is small. However, in table 3 is shown that compared with a tube of radius 2 mm ( $Bo = 0.54$ ), a slightly lower average tip speeds is acquired, which is caused by the effect of gravity.

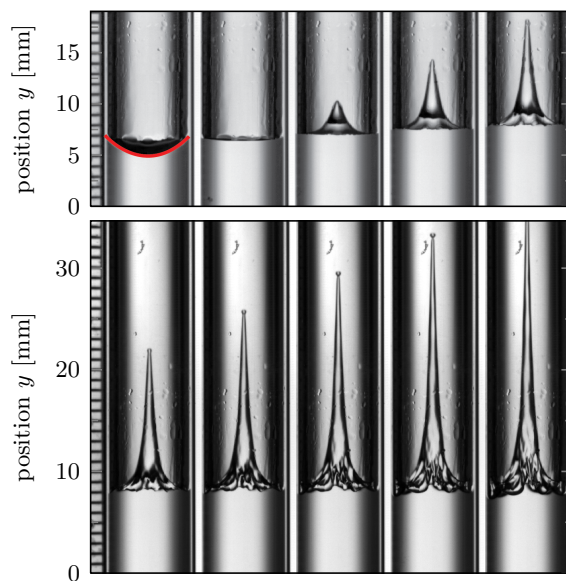


Figure 12: Image sequence as recorded by a high-speed camera at a framerate of  $40 \times 10^3$  FPS for an experiment with  $U_C = 1700$  V and  $d = 8$  mm. The time interval separating each frame of this sequence is  $\Delta t = 0.2$  ms, where at frame  $t_2$  the pressure pulse had just hit the free surface.

As can be seen, the fluid flow is focussed towards the centre, which enables the jet formation. Figure 13 and 14 show the same experiment, but for different contact angles. Because the coating procedure resulted in a non-homogeneous coating, the meniscus was not always axisymmetric, resulting in a non-axisymmetric jet, therefore figures 12 to 14 show radial curvatures on the jet.

Figure 15 shows how tip speed changes with variations in contact angle. It shows that the theoretical relation of Tagawa *et al.* (2012) is better than the curvature relation of Antkowiak *et al.* (2007) for the experiment performed in this thesis. The fitting constants for the relation  $v_{\text{tip}} = C_1(1 - \sin \theta) + C_2$  are  $C_1 = 12 \text{ m s}^{-1}$ ,

## 4. Experimental results and Discussion

---

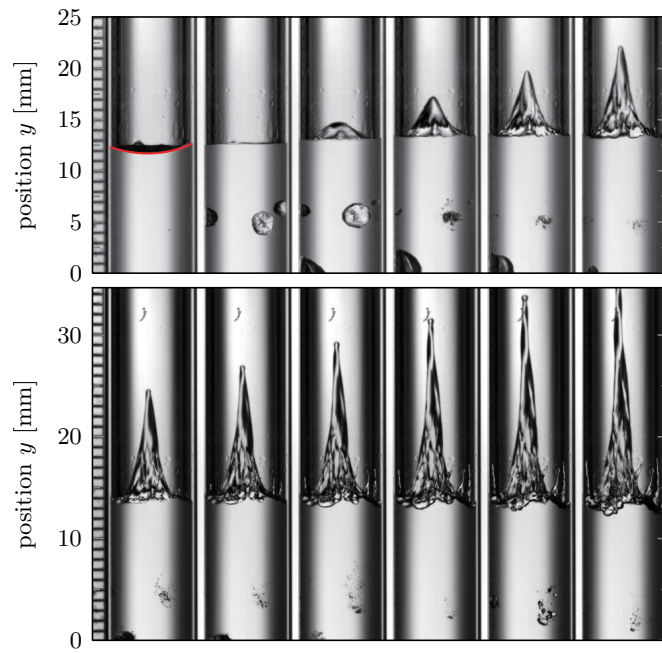


Figure 13: Same settings as in figure 12, but a lower contact angle.

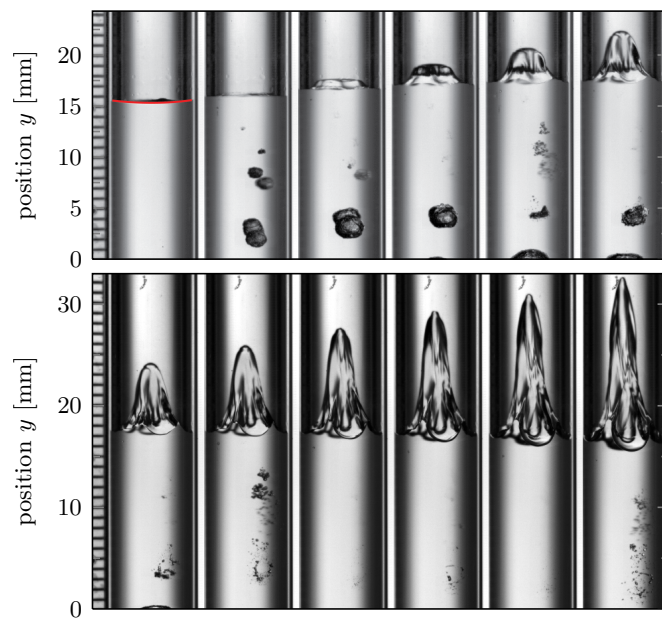


Figure 14: Same settings as in figure 12 and figure 13 but an even lower contact angle.

and  $C_2 = 10 \text{ m s}^{-1}$ . For this pressure record it means that the effect of curvature is higher than the effect of the absolute pressure for the tip speed. The relation  $v_{\text{tip}} = C_1(1 + \beta \cos \theta)$  results in fitting constants of  $C_1 = 4.8 \text{ m s}^{-1}$ , and  $\beta = 2.9$ . This means that according to this theory, again the effect of curvature is higher, but it is also higher relative to the previous theory of Antkowiak et al.

Figure 11 shows that the influence of the contact angle is proportional to the absolute pressure, and that the two mechanisms can be decoupled.

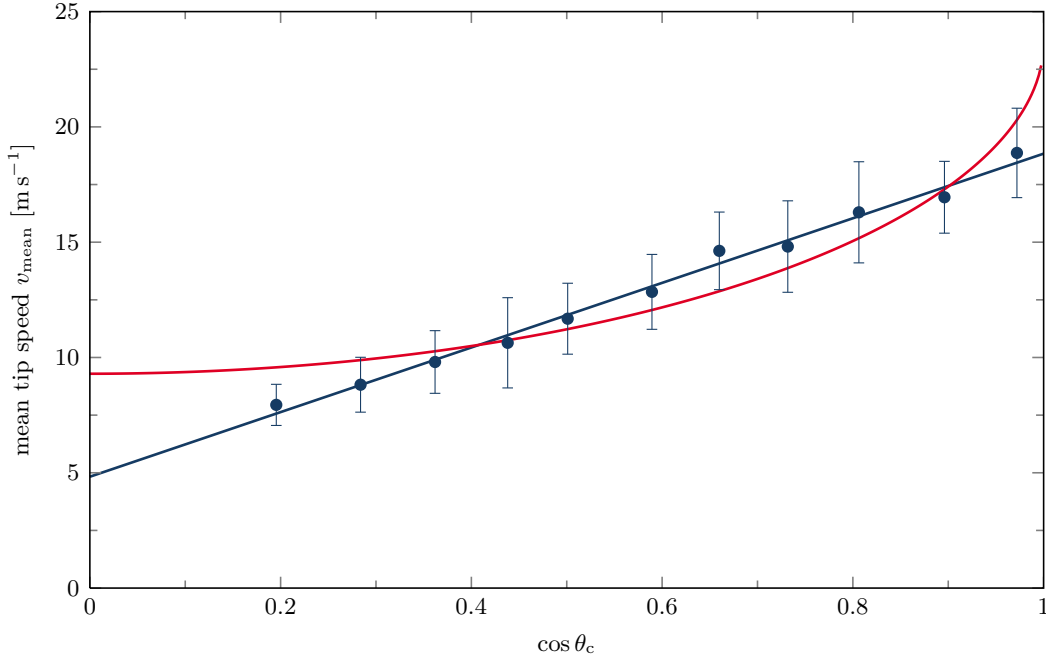


Figure 15: Comparison of experiment (●) and two theories, namely  $1 - \sin \theta_c$  (—) and  $1 + \beta \cos \theta_c$  (—) on the relation between jet tip speed and contact angle  $\theta_c$  at constant voltage  $U_C = 1800 \text{ V}$ . The plot is based on 200 single experiments and the error bar indicates the sample standard deviation for each data point.

### 4.4. Effect of tube radius on tip speed

To study the effect of diameter on the tip speed, several experiments have been performed with uncoated tubes, thus  $\theta_c = 0^\circ$ , because that contact angle was reproducible, and created axisymmetric jets, in contrary to experiments with coated tubes. According to the theory the tip speed should not depend on diameter for the experiment in this thesis. This is confirmed in table 3, where for two different  $U_C$  and two tube radii the resulting mean tip speed is shown. A very small decrease in mean speed is found for increasing tube radius, which is likely caused by the effect of gravity, which flattens the free meniscus and thereby reduces its average curvature. It is explained in the appendix (A.2.1) that is such a case the contact

#### 4. Experimental results and Discussion

---

angle will not be sufficient to describe the focusing effect with an example of a tube radius of 12 mm. However, the sample standard deviation for the measurements shows that this decrease in mean speed is not significant compared to the sample standard deviation.

|                          | R = 2 mm                          | R = 4 mm                          |
|--------------------------|-----------------------------------|-----------------------------------|
| $U_C = 1400 \text{ V}$ : | $(5.8 \pm 2.7) \text{ m s}^{-1}$  | $(4.9 \pm 1.9) \text{ m s}^{-1}$  |
| $U_C = 1800 \text{ V}$ : | $(13.7 \pm 5.6) \text{ m s}^{-1}$ | $(13.3 \pm 2.9) \text{ m s}^{-1}$ |

Table 3: Values of mean tip speed,  $v_{\text{mean}}$ , at constant contact angle,  $\theta_c = 0^\circ$ , different voltage,  $U_C$ , as well as tube radius, R. The table is based on 120 single experiments and the uncertainty indicates the sample standard deviation for each data point.

### 5. Future work

Using this experimental system one could further expand the measurements done to validate the given theories. Another parameter, next to the tip speed of the jet, namely the volume flow at different heights might give a good description of the focusing effect, because it directly takes into account the radial profile of the jet. It is very likely also an important parameter in future applications of jets in for example needle-free injections and fuel-injection systems. It would also be interesting to perform experiments with different fluids to see to which extent the theoretical relation for the jet speed still applies. Next to that, high-speed visualization of the pressure pulse, using for example a high-speed Schlieren technique, could greatly increase the understanding of the effect of the pressure pulse on the jet formation. Investigation of the secondary jet shown in the side experiments (appendix A) can provide insight into the reflections that happen on the glass tube/steel tube transition. It can also provide a further insight into the role of shock waves induced by collapsing vapour bubbles. A better visualisation of the vapour bubbles beneath the liquid surface will make it possible to verify if their location and size is the same between experiments as expected from the side experiments. Simulations can provide a tool to analyse the reflections of the pressure pulse when a small tube with a free surface is placed inside a big tube, like in our experiment. The free surface flows of the jet generation can be investigated by using a (3D) particle tracking technique, for example particle image velocimetry (PIV).

## 6. Conclusion

The dynamics of focused tubular jets have been studied for tubes ranging from 2 mm to 4 mm in radius. Liquid jets have been created using a shocktube setup, and the pressure pulse - accounting for the jet generation - was measured with two PVDF sensors flush mounted on the tube's wall. This setup allowed for reproducible jets with speeds up to  $50 \text{ m s}^{-1}$ . Using high-speed imaging, the evolution of the jet was captured for different meniscus shapes and pressure amplitudes. The jet formation was captured using a high-speed camera at framerates ranging from  $16 \times 10^3 \text{ FPS}$  to  $50 \times 10^3 \text{ FPS}$ . Reflection of the pressure pulse creates vapour bubbles beneath the free surface. These bubbles are reproducible in place and time according to the side experiments shown in the appendix (A.2.4).

The effect of the control parameters, namely tube radius, contact angle ( $\theta_c$ ), and amplitude of the pressure pulse on the speed of the jet tip has been investigated in a series of experiments. Using models of Antkowiak *et al.* (2007) and Tagawa *et al.* (2012), the relation between contact angle and tip speed has been investigated. The experiments showed that tip speed scales with the latter model, namely  $1 + \beta \cos \theta_c$ . Linear acoustic theory, or more precisely the particle velocity derived from it, gives a good prediction of the effect of tube radius and the amplitude of the pressure pulse on tip speed for the investigated parameter range. The effect of a change in tube radius is shown to be negligible, whereas the amplitude of the pressure pulse is proportional to the tip speed of the jet. This corresponds with the prediction of linear acoustic theory. A combination of linear acoustic theory and the contact angle dependency leads to good agreement with the measurements. In the appendix (A.2), side experiments and possible future projects are shown.

### Acknowledgements

Many people were involved in the process of completing this thesis. I would like to thank first of all my girlfriend Kim, and my parents, Agnes and Jos. Because of their indefatigable support I can write these words in my graduation thesis. I would like to express my gratitude to an important person, for he initiated this research and will continue it for his Ph.D., Alexander Klein. He was my supervisor during the internship at Bosch and my companion during the quest for knowledge for a period of in total more than a year. Various interesting topics were addressed in our talks, from physical nature, such as absolute negative pressures and jet formation, to practical nature, for example the implementation of a great number of measurement devices and techniques, and helpful matlab or latex programs. This research has been carried out in the Physics of Fluids group of the Faculty of Science and Technology of the University of Twente. I would like to thank my supervisor Dr. Chao Sun, my secondary supervisor Dr. Yoshiyuki Tagawa, Prof. Dr. Ir. Leen van Wijngaarden, Prof. Dr. Andrea Prosperetti, Dr. Devaraj van der Meer, and of course Prof. Dr. Detlef Lohse, chair of the PoF group for the interesting discussions we had and for the facilities that I could use. Thanks to my neighbour members of the research group, because of the joy they could give during the work with small talk about all kinds of subjects, but also because of the in-depth discussions on relevant topics for my research and common knowledge. A special thanks is for the students of ME236, Oscar Bloemen, Nikolai Oudalov, Erwin van der Poel, Matthias van de Raa, and Roeland van der Veen. Also I would like to thank Robert Bosch, GmbH for they provided the funding for the experimental setup and transport to and from Enschede. During the research a lot of discussion has taken place with Nikolai Oudalov, who conducted jet experiments on micro-scale with tubes of  $50\ \mu\text{m}$  to  $500\ \mu\text{m}$  in diameter.

### References

- ANTKOWIAK, A., BREMOND, N., LE DIZÈS, S. & VILLERMAUX, E. 2007 Short-term dynamics of a density interface following an impact. *Journal of Fluid Mechanics* **577**, 241.
- BERGMANN, RAYMOND, DE JONG, ERIK, CHOIMET, JEAN-BAPTISTE, VAN DER MEER, DEVARAJ & LOHSE, DETLEF 2008 The origin of the tubular jet. *Journal of Fluid Mechanics* **600**, 19–43.
- BLAKE, J.R. & GIBSON, D.C. 1987 Cavitation bubbles near boundaries. *Annual Review of Fluid Mechanics* **19**, 99–123.
- CAUPIN, F & HERBERT, E 2006 Cavitation in water: a review. *Comptes Rendus Physique* **7**, 1000–1017.
- COLE, R.H. 1948 *Underwater explosions*. New Jersey: Princeton University Press.
- CONCUS, PAUL 1968 Static menisci in a vertical right circular cylinder. *Journal of Fluid Mechanics* **34** (part 3), pp. 481–495.
- DUCHEMIN, LAURENT, POPINET, STEPHANE, JOSSERAND, CHRISTOPHE & ZALESKI, STEPHANE 2002 Jet formation in bubbles bursting at a free surface. *Physics of Fluids* **14** (9), 3000.
- EGGERS, JENS & VILLERMAUX, EMMANUEL 2008 Physics of liquid jets. *Reports on Progress in Physics* **71** (3), 036601.
- GEKLE, S. & GORDILLO, JM 2010 Generation and breakup of Worthington jets after cavity collapse. Part 1. Jet formation. *Journal of Fluid Mechanics* **663**, 293–330.
- GEKLE, STEPHAN, GORDILLO, JOSÉ, VAN DER MEER, DEVARAJ & LOHSE, DETLEF 2009 High-Speed Jet Formation after Solid Object Impact. *Physical Review Letters* **102** (3), 1–4.
- DE GENNES, PIERRE-GILLES, BROCHARD-WYART, FRANCOISE, BROCHARD-WYART, QUERE & BROCHARD-WYART, DAVID 2004 *Capillarity and Wetting Phenomena*. Springer.
- GORDILLO, J. M. & GEKLE, STEPHAN 2010 Generation and breakup of Worthington jets after cavity collapse. Part 2. Tip breakup of stretched jets. *Journal of Fluid Mechanics* **663**, 331–346.
- GREENSPAN, M & TSCHIEGG, C E 1982 Radiation-induced acoustic cavitation; Threshold versus temperature for some liquids. *Technical Notes and Research Briefs, Journal of Acoustical Society America* **72**, 1327–1331.

- HERBERT, E, BALIBAR, S & CAUPIN, F 2006 Cavitation pressure in water. *Physical review E* **74**, 1–22.
- VAN HOEVE, WIM, GEKLE, STEPHAN, SNOEIJER, JACCO H., VERSLUIS, MICHEL, BRENNER, MICHAEL P. & LOHSE, DETLEF 2010 Breakup of diminutive Rayleigh jets. *Physics of Fluids* **22** (12), 122003.
- KAWAI, HEIJI 1969 The piezoelectricity of Poly (vinylidene Fluoride). *Japanese Journal of Applied Physics* **8**, 975.
- KEDRINSKII, VALERY K. & TRANSLATED BY SVETLANA YU. KNYAZEVA 2005 *Hydrodynamics of Explosion - Experiments and Models*. Springer-Verlag.
- LIN, S. P. & REITZ, R. D. 1998 Drop and Spray Formation From a Liquid Jet. *Annual Review of Fluid Mechanics* **30** (1), 85–105.
- LONGUET-HIGGINS, M. S. 2006 Bubbles, breaking waves and hyperbolic jets at a free surface. *Journal of Fluid Mechanics* **127**, 103.
- MADER, C.L. 1965 Initiation of detonation by the interaction of shocks with density discontinuities. *Physics of Fluids* **8** (10), 1811.
- MATLAB 2008 The Mathworks - The Language Of Technical Computing [<http://www.mathworks.com/products/matlab/>]. Online in Internet: `\url{http://www.mathworks.com/products/matlab/}`.
- MCWILLIAM, D. & DUGGINS, R.K. 1969 Speed of sound in bubbly liquids. *Proceedings of the Institution of Mechanical Engineers* **184** (3C), 102–107.
- MONAHAN, E.C. & MAC NIOCAILL, GEAROID 1986 *Oceanic Whitecaps - And Their Role in Air-Sea Exchange Processes*. Springer.
- MORSINK, GERBEN J. 2010 Tensile Strength in Liquids. *Tech. Rep.*. University of Twente.
- O'BRIEN JR., W.D. 1998 Assessing the risks for modern diagnostic ultrasound imaging. *Jpn. J. Appl. Phys. Vol* **37**, 2781–2788.
- OGUZ, H.N. & PROSPERETTI, A. 1993 Dynamics of bubble growth and detachment from a needle. *Journal of Fluid Mechanics* **257**, 111–111.
- ODALOV, NIKOLAI 2011 Supersonic microjet generation using laser-induced vapour bubble. PhD thesis, University of Twente.
- PETERS, IVO 2011 Private communications.
- PLATEAU, J. A. F. 1873 Statique Expérimentale et Théorique des Liquides Soumis aux Seules Forces Moléculaires. *Gauthier-Villard, Paris* .

## References

---

- RAYLEIGH, L. 1879 On the capillary Phenomena of Jets. *Proc. R. Soc. London* **29** (71).
- REYNOLDS, DOUGLAS D. 1981 *Engineering Principles in Acoustics*. Boston: Allyn and Bacon Inc.
- SUN, CHAO, CAN, EDIP, DIJKINK, RORY, LOHSE, DETLEF & PROSPERETTI, ANDREA 2009 Growth and collapse of a vapour bubble in a microtube: the role of thermal effects. *Journal of Fluid Mechanics* **632**, 5.
- TAGAWA, YOSHIYUKI, OUDALOV, NIKOLAI, VISSER, CLAAS-WILLEM, PETERS, IVO, VAN DER MEER, DEVARAJ, SUN, CHAO, PROSPERETTI, ANDREA & LOHSE, DETLEF 2012 On highly focused supersonic microjets, to be published. *Journal of Fluid Mechanics* .
- TEMPERLEY, H N V & TREVENA, D H 1979 Metastable effects associated with the reflection of a pressure pulse at the free surface of water. *J. Phys. D: Appl. Phys.* **12**, 1887–1894.
- THOMPSON, P.A. 1971 *Compressible-Fluid Dynamics*. McGraw-Hill Inc.
- THURAISINGHAM, RA 1998 Sound speed in bubbly water at megahertz frequencies. *Ultrasonics* **36** (6), 767–773.
- VELDHUIS, CHRISTIAN 2006 Leonardo’s paradox. PhD thesis, University of Twente.
- WALTERS, W.P. & ZUKAS, J.A. 1989 *Fundamentals of Shaped Charges*. New York: Wiley.
- WILLIAMS, P R & WILLIAMS, R L 2002 Cavitation of liquids under dynamic stressing by pulses of tension. *J. Phys. D.: Applied Physics* **35**, 2222–2230.
- YOUNG, F.R. 1989 *Cavitation*. London: McGraw-Hill Inc.
- ZHU, SONGLIN, COCKS, FRANKLIN H, PREMINGER, GLENN M & ZHONG, PEI 2002 The role of stress waves and cavitation in stone comminution in shock wave lithotripsy. *Ultrasound in Medicine & Biology* **28** (5), 661–671.
- ZIJLSTRA, AALDERT 2007 Jets from finite-wave free-surface reflections. PhD thesis, University of Twente.
- ZIJLSTRA, AALDERT & OHL, CLAUS DIETER 2008 On fiber optic probe hydrophone measurements in a cavitating liquid. *The Journal of the Acoustical Society of America* **123** (1), 29–32.

## A. Appendix

The preliminary results of the boundary integral code is shown in appendix A.1. A lot of work has been done to investigate on possible boundaries or uncommon implications of the theories that are shown in this report. A list of these jet-related phenomena is given in appendix A.2. This list can be used as a guide for exploring phenomena related to the type of jet formation studied in this report, such as surface waves for high Bond number, contact angles equal or bigger then  $90^\circ$ , moving menisci, cavitation, defocussing and more. Next, a high-speed pressure pulse visualization technique, namely Schlieren, and some pitfalls are shown in appendix A.3. Future experimenters are further referred to section A.4 for a proof that the most dangerous cleaning method may not prove to be the best.

### A.1. Boundary integral simulations

Figure 16 shows an overlay of the experimental observed shape after correcting for refraction and deviations from axisymmetry, and the contour of the boundary integral simulations. An excellent agreement is observed.

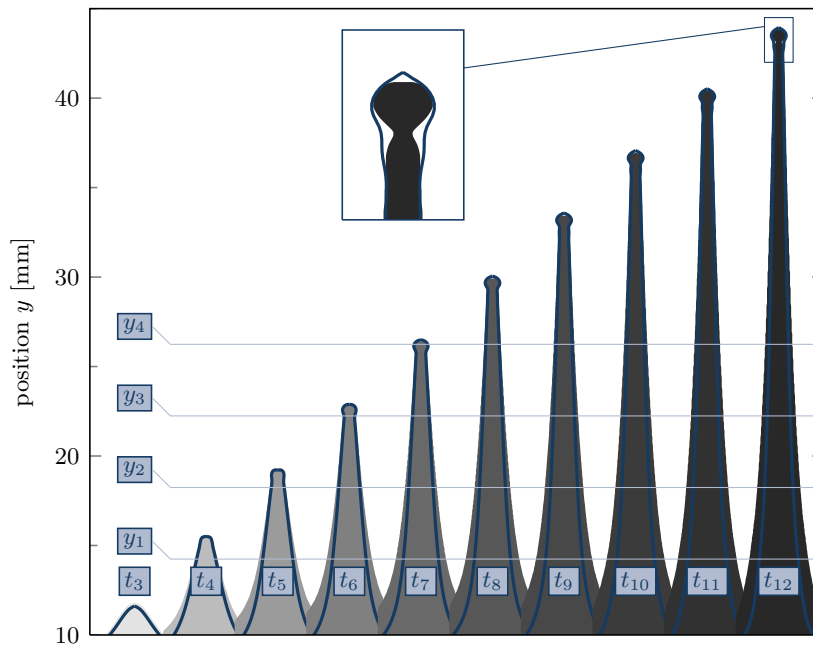


Figure 16: The shaded area represents the digitallly processed image sequence of figure 6 and the line represents the the contour of the BI simulations. The digitallly processed images contain the refraction correction and are obtained from the chord-length parametrisation of the jet.

## A. Appendix

### A.2. Side experiments and possible future projects

Several phenomena are not investigated upon in enough detail to provide quantitative results. A qualitative description of the phenomena with a possible direction for future work is given. These examples show what can be expected if some of the boundaries of the theories used in this work are trespassed.

#### A.2.1. Higher Bond numbers

For higher Bond numbers gravity has an clear effect on the meniscus shape. In that case, the meniscus shape must be fitted using the Young-Laplace equation, which has to use the general expressions for the curvature, like in equation 11. Using this fit a good approximation of the contact angle with the wall can be found. In this section a tube of 24 mm is considered, which was sealed on the steel tube. In figure

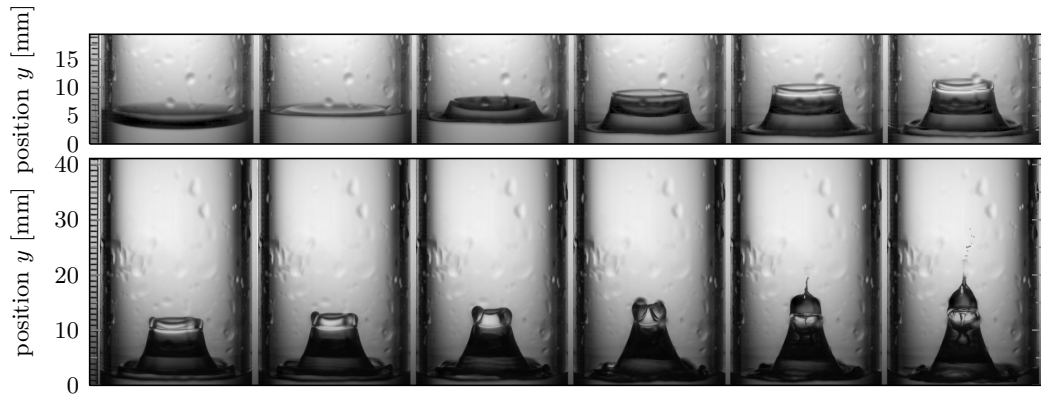


Figure 17: Image sequence as recorded by a high-speed camera at a framerate of  $10 \times 10^3$  FPS for an experiment with  $U_C = 1650$  V and  $d = 24$  mm. The time interval separating each frame of this sequence is  $\Delta t = 1$  ms, where just after frame  $t_1$  the pressure pulse hits the free surface.

17 is shown that, after a shockwave had hit the free surface, wave-like jets grow at the sides. They are directed upwards and inwards. After 9 ms they collapse, at which point an air cavity is formed. Because the collapse leads to the entrapment of an air bubble, a singular jet is created, like the one described by Gekle *et al.* (2009). This jet has a much higher speed than expected from the momentum of the waves. It gets an extra push from the capillary force, which also creates a downwards moving jet to conserve momentum. The points of highest curvature on the meniscus resulted in the fastest fluid flow after impact of the pressure pulse. A possible way of modelling this is by dividing the tube in two sections, a flat one (figure 18a) and a curved one (figure 18b). By studying this case of (relatively) high Bond number, more information is also obtained for the transition region from low to high Bond number. In this region the phenomena can not be clearly visualised,

but the tip speed is expected to be lower.

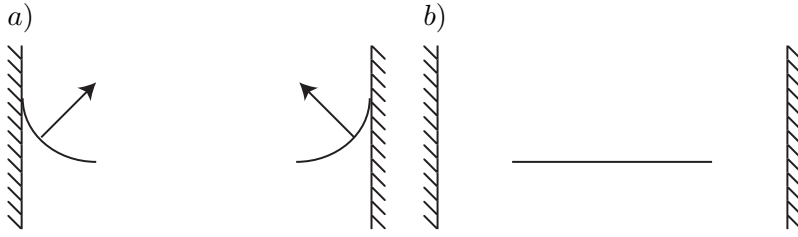


Figure 18: Division of a meniscus with high Bond number into: a) high curvature region and b) no curvature region.

### A.2.2. Flat free surface

A pressure pulse which is shot on a flat surface moves the liquid column up as a whole, as shown in figure 19. The concave part of the free surface at the center top of the column is surrounded by a growing convex part, a 'wave', until the concave part will only exist of a single point; a singularity. This singularity will result in a fast, thin, sharp, jet, like the singular jet described by multiple authors (Bergmann *et al.*, 2008; Gordillo & Gekle, 2010; Gekle & Gordillo, 2010). A small asymmetry of the liquid column will result in a singular jet that is not moving perfectly vertical.

### A.2.3. A convex free surface

A free surface with  $\theta_c > 90^\circ$  will not create a liquid jet like the ones discussed so far in this thesis when a pressure pulse hits it. As can be seen in figure 20, for a  $\theta_c$  of  $105^\circ$ , instead of the normal jet formation, a rise of the liquid close to the wall is observed. This creates a nearly flat meniscus in the centre of the tube in frames  $t_2$  and  $t_3$ . Starting from frame  $t_4$  the movement of the base of the meniscus has changed from upwards to downwards. The time between the start of the base movement and the change of direction is 2 ms, if the trend in the paper of Sun *et al.* is continued, the radius of the vapour bubbles would be in the order of  $1000 \mu\text{m}$  if heat would be important in the process of creating vapour bubbles (Sun *et al.*, 2009). However, it is not expected that heat is important. A better understanding of the vapour bubbles created when the pressure pulse is reflected as a tension wave will help to influence the pumping effect. The pumping effect caused by the vapour bubble will likely have an influence on the volume flow of the jet. Simultaneously a jet-like shaped disturbance appears in the centre of the tube, which has two possible reasons: inertia or the hit of shockwaves induces by collapsing bubbles. Frame  $t_8$  shows a concave formed ring around the disturbance, that creates a real 'ring-shaped' jet that already collapsed together in frame  $t_9$ , while the disturbance still travelled downwards. The collapsed 'ring-shaped' jet travels further up in frames  $t_{10}$  to  $t_{12}$ .

Because initially the meniscus is static, the Young-Laplace equation must hold. This indicates that the possibility of a small concave ring close to the wall which

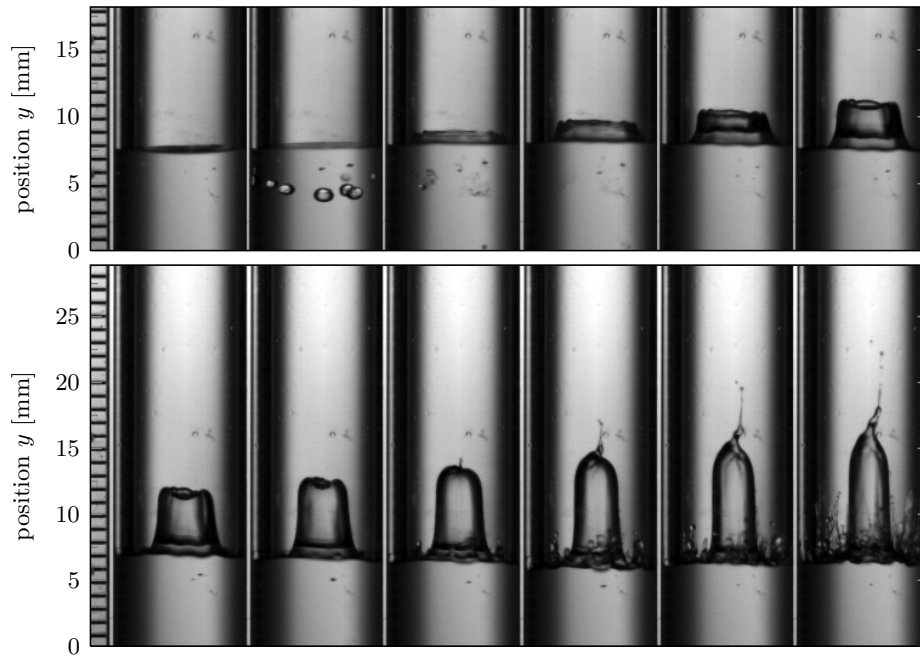


Figure 19: Image sequence as recorded by a high-speed camera at a framerate of  $50 \times 10^3$  FPS for an experiment with  $U_C = 1500$  V and  $d = 8$  mm. The time interval separating each frame of this sequence is  $\Delta t = 0.42$  ms. The image sequence shows a 'two-step' jet.

focusses the liquid flow into a 'ring-jet', such as seen in the 21 falls of. This implicates that the effect observed here is the defocussing of a convex meniscus, which directs the fastest liquid towards the wall. The explanation of this follows from potential theory, because for a convex meniscus the vertical pressure gradient is higher close to the walls, which leads to higher vertical velocities at the walls than in the centre. It leads to a paradoxical situation: hydrophobic walls will lead to more fluid flow towards the wall, compared with hydrophilic walls, when a pressure pulse is shot on a meniscus. The hydrophobicity of the glass wall is not homogeneous and is likely to increase with height, because of effects described at section 3.4. Despite of this, the liquid film that is created at the glass wall exists for more than  $7.5 \mu\text{s}$ , after which it gets distorted by droplets, impacting on the tubes wall. It is expected that for more hydrophobic surfaces, the flow that is focussed towards the wall might bounce back or breakup otherwise. Because of the focus towards jet formation, this phenomena has only been observed once. However, it has also been observed on a different scale (Oudalov, 2011).

#### A.2.4. Ring jet formation

The meniscus to create the secondary ring jet, shown in figure 21, has a contact angle of  $20^\circ$ . Frame  $t_1$  to  $t_4$  show the jet formation. This jet alters the shape of the base of the meniscus, and the lowest point becomes ring-shaped. Then, from frame  $t_4$  onwards, a ring jet is observed. To the ring jet will also be referred to in this section as the secondary jet. To understand the mechanism for the ring jet generation better, the pressure pulse, as measured by two PVDF pressure sensors, is shown in figure 22. First the pressure pulse moves up. Two peaks are found, first of the pressure transducer at height 0.375 m, then of the pressure transducer of height 0.775 m. The extrapolated time of where the pressure pulse hits the surface at height 1.1 m is shown as  $t_{ap}$  in the figure, using a calculated propagation velocity of  $1450 \text{ m s}^{-1}$ . The two times where the reflection at the free surface is seen in the image sequence are denoted  $t_{i1}$  and  $t_{i2}$  and have a red line. The time of the first reflection at the free surface that is found by extrapolating the propagation of the pressure pulse agrees very well with the time where the jet creation is observed. After the reflection at the top, a downgoing pulse is expected, first in the upper transducer (—,  $t_{r2}$ ), then at the lower transducer (—,  $t_{r1}$ ). This reflection is not seen in the pressure plot at the expected time, but at a much later time, around  $t = 4 \mu\text{s}$ . The distance the pressure pulse would have traveled at that time is five times the tube length, plus the distance from the free surface to the pressure sensor. The argument that a reflection would not be measured, because the pressure pulse does not expand in the steel tube, and that therefore the sensors at the wall cannot measure it falls off, because a reflection is measured. Another explanation of propagation of the pressure pulse is given next. The expected time when the reflected pulse from the bottom hits the free surface again, according to a propagation at a constant speed of  $1450 \text{ m s}^{-1}$  is at time  $t_{rb}$ . Not at this time, but at a later time  $t_{i2}$ , the reflection is observed with the high-speed images, because it generates the second ring-shaped

## A. Appendix

---

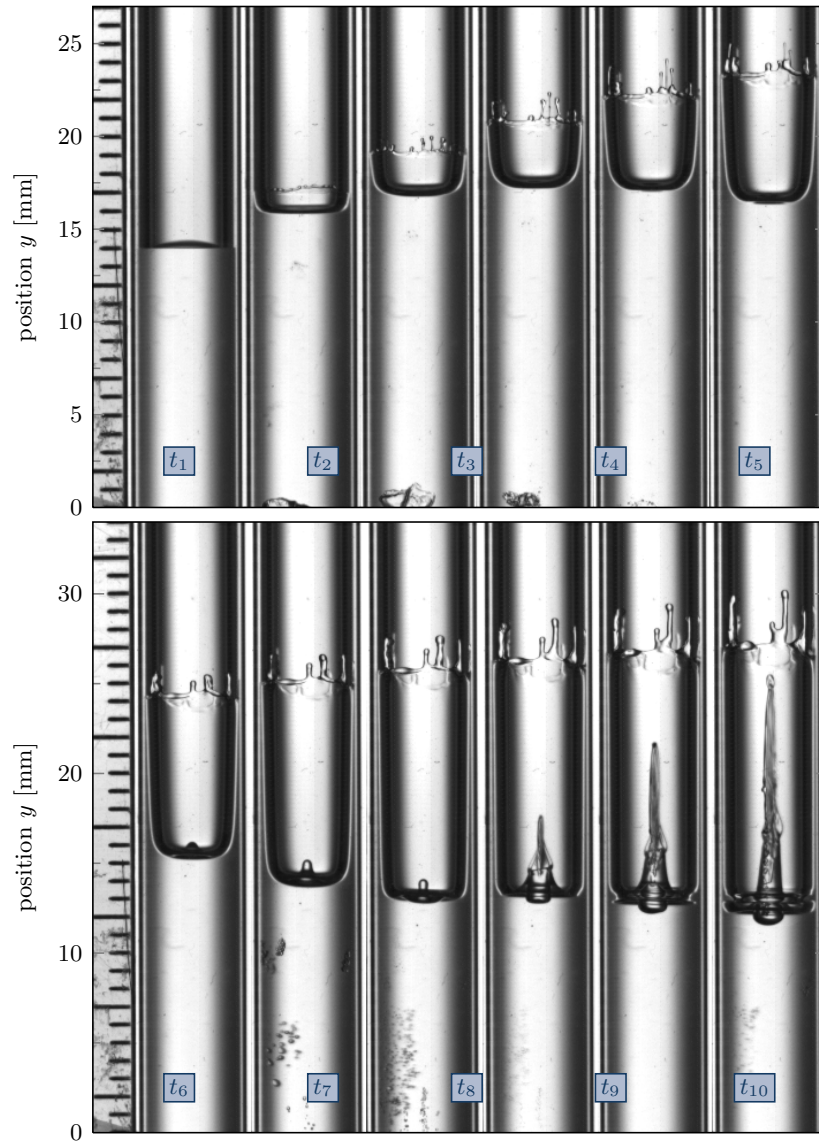


Figure 20: Image sequence as recorded by a high-speed camera at a framerate of  $40 \times 10^3$  FPS for an experiment with  $U_C = 1700$  V and  $d = 6$  mm. The time interval separating each frame of this sequence is  $\Delta t = 0.35$  ms. The initial meniscus has a  $\theta_c$  of  $105^\circ$ , which makes it convex.

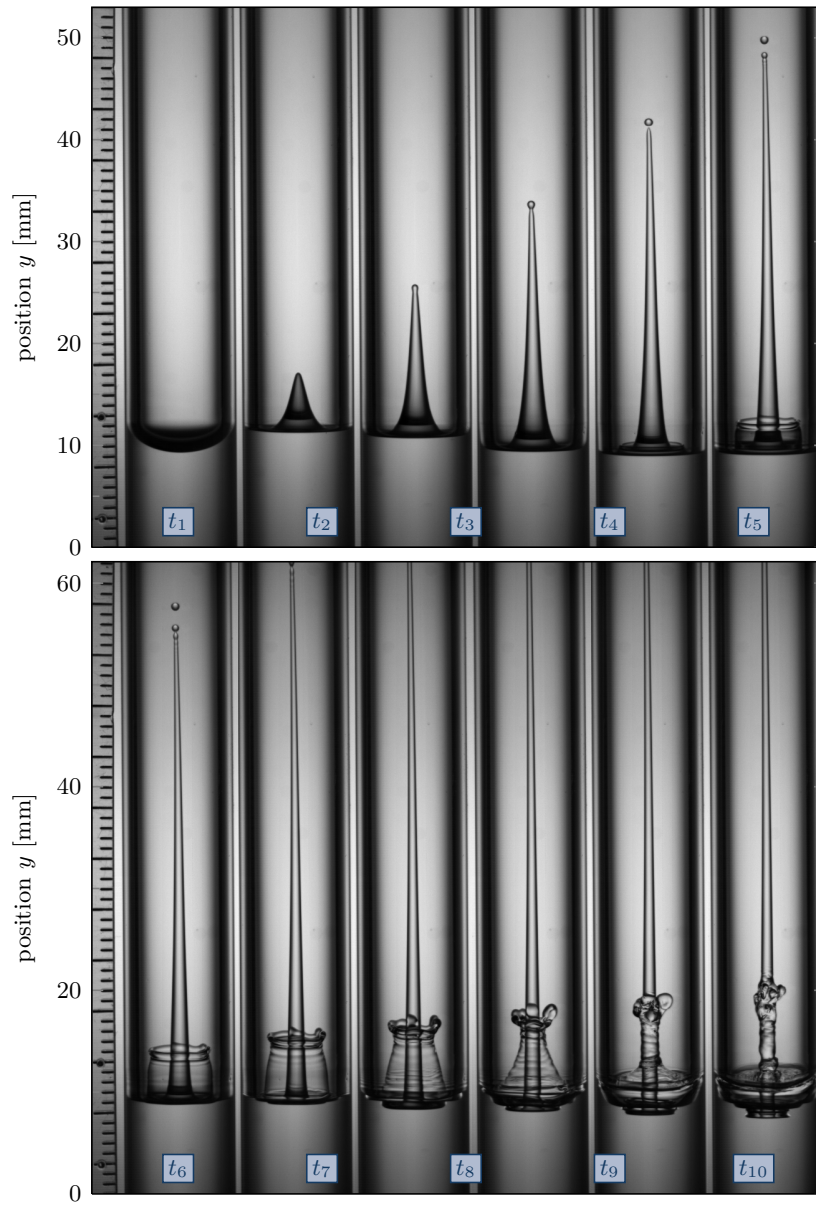


Figure 21: Image sequence as recorded by a high-speed camera at a framerate of  $16 \times 10^3$  FPS for an experiment with  $U_C = 1450$  V and  $d = 8$  mm. The time interval separating each frame of this sequence is  $\Delta t = 0.875$  ms. Starting from frame  $t_4$  a ring jet is observed.

## A. Appendix

jet. Because no pressure pulse is measured with the sensors that could be directly responsible for this jet generation, and because  $t_{i2}$  does not correspond with  $t_{rb}$ , this leads to the conclusion that another effect than the reflection of the pressure pulse at the bottom of the tube is responsible for the second jet generation at time  $t_{i2}$ . The

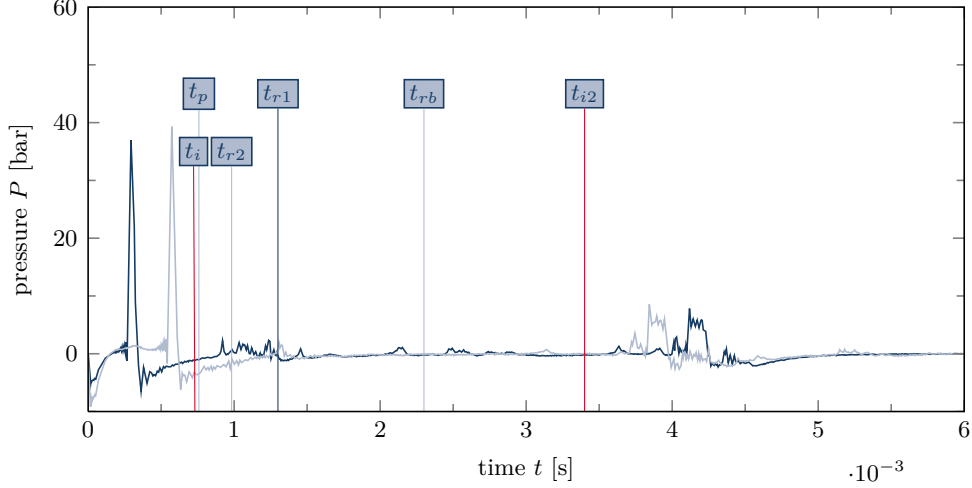


Figure 22: Simultaneous pressure record of two PVDF pressure transducers at different positions during the jet creation shown in figure 21. The distance of the transducer to the copper disc at the tube's bottom is 0.375 m for transducer 1 (—) and 0.775 m for transducer 2 (---). The total height of the liquid column is  $\sim 1.10$  m. The propagation speed of the initial pressure pulse based on the time delay of both signals is estimated to  $1450 \text{ m s}^{-1}$ . This leads to a propagation delay of the pressure pulse from the measuring point to the free surface of about 0.6 ms and 0.3 ms for transducer 1 and 2, respectively. The estimated arrival time of the pressure pulse, based on the propagation velocity, is  $t_p = 0.76 \mu\text{s}$ . The arrival time of pressure pulse was between  $0.72 \mu\text{s} < t_i < 0.78 \mu\text{s}$ , based on the image sequence. Based on a reflection at the bottom, and constant propagation velocity, the second reflection would hit the surface at  $t_{rb} = \frac{3.3 \text{ m}}{1450 \text{ m s}^{-1}} = 2.3 \text{ ms}$ . However, at  $t_{ai}$ , then the second jet is generated.

reasoning for the reflection that causes the ring jet comprises of two steps. The first step concerns reflections at point b) of figure 23. Because the radius of the steel tube is larger than that of the glass tube, the pressure pulse does not get reflected when it moves into the glass tube. However, after the wave is reflected at the free surface the pressure pulse moves from a small tube to a big tube. This will create a (partly) reflected pressure pulse, which will hit the surface again. This might be the reason why no reflected pressure pulse is seen. However, it does not explain why  $t_{ib} > t_{rb}$ , rather the opposite. To study the reflective behaviour of the pressure pulses in this experimental setting it is recommended to do a numerical study, combined with visualization of the pressure pulse, using for example a Schlieren technique. The second step concerns the collapse of vapour bubbles. Vapour bubbles are often seen in the form of a cavitation layer beneath the meniscus. This is because at a

certain point beneath the surface the tension in the liquid becomes high, due to the negative pressure of the reflected pulse, which stimulates the cavitation of the liquid. Vapour bubble could also exist at a much lower point in the experimental setup, because of the reflective behaviour explained in step one. Simulations of different geometries have shown that the pressure can greatly decrease at certain points in a setup where multiple reflections play a role, such as expected between point a) and c), because of superposition. Next, two things happen. Because of vapour bubbles, the speed of the pressure pulse drastically decreases. Even values lower than the speed of sound in air are possible (McWilliam & Duggins, 1969; Thuraisingham, 1998). Also, the base of the jet will move, thereby depending on the size of the vapour bubbles. At  $t_{ai}$ , the base stops moving down. This is a sign that the bubbles have collapsed and therefore the liquid column cannot move down anymore. These collapsing bubbles will create a shockwave that travels up to the surface. It might also be the moment that the reflected pressure pulse finally reaches the free surface again through the liquid, full of vapour bubbles. This generation of the secondary jet is highly reproducible. For a given geometry, the reflections of the pressure pulse will also be equal. Therefore the bubble generation might be reproducible in time and location as well.

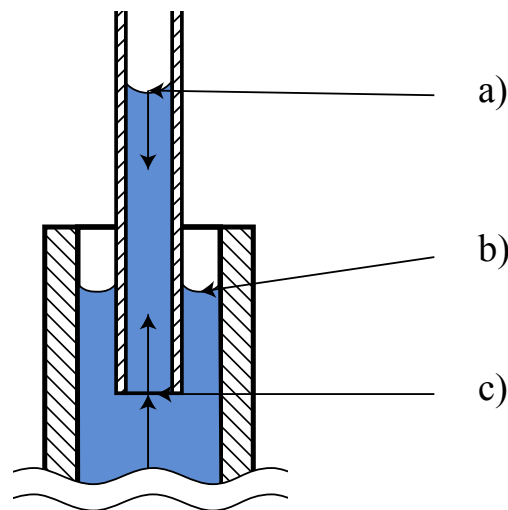


Figure 23: Schematic diagram of the experimental setup with the points of reflection. First the pressure pulse moves into the small tube without reflecting. Next, the pressure pulse reflects at the free surface. Then, it will reflect at the point where the small tube ends. In the end a superposition of several upwards and downwards moving pulses will occur between point a) and c).

#### A.2.5. Small air bubbles at the free surface

In figure 24 multiple small bubbles are located at the free surface, close to the wall. As can be seen in frame 2, a normal jet is created initially, next to some very small

## A. Appendix

---

jets created at the bubbles. Later frames show that the whole jet gets distorted due to the distortion of the free surface which already started at frame 2. Frame 3 also shows that the fastest liquid in this case is initiated at the small bubbles and not in the middle of the tube. Another difference is that the bubbles are close to the wall, so the wall might have a more pronounced effect on the jet creation by the bubbles. In the theory section (2.2), multiple theories are explained which only include the contact angle and not the curvature.

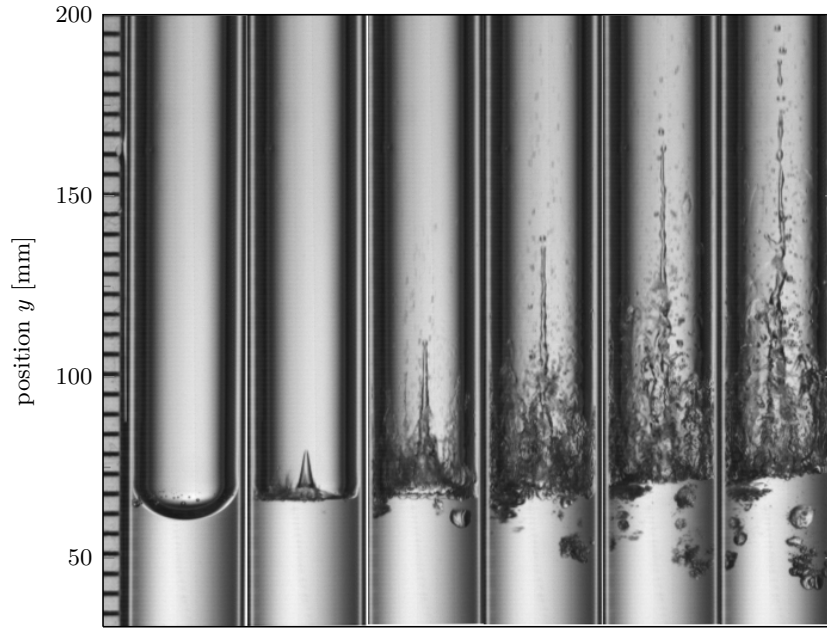


Figure 24: Image sequence as recorded by a high-speed camera at a framerate of  $50 \times 10^3$  FPS for an experiment with  $U_C = 2050$  V and  $d = 4$  mm. The time interval separating each frame of this sequence is  $\Delta t = 0.4$  ms. At the left, close to the wall, a small bubble is visible.

### A.2.6. A big air bubble beneath the free surface

Figure 25 shows at time  $t_1$  the fluid at rest. A big bubble is located  $\sim 1.5$  cm below the free surface. At time  $t_2$  the pressure pulse has hit the bubble. The next frame,  $t_3$ , shows a donut shaped cavitation that moves up and the top meniscus is also moving up. In frame  $t_4$  the donut-shaped cavitation layer got followed by a bigger region of cavitation. Interesting is that the top of the bubble is relatively unharmed by the impact of the jet, also in later frames. Note that the absolute pressure of this shot is relatively high, (2500 V corresponds to almost 100 bar peak pressure according to figure 4). Therefore the part of the pressure pulse that continues through the air of the bubble and the top layer of liquid still has enough energy to generate a slow jet at the top in frame  $t_3$  to  $t_12$ . This jet not goes straight up, but hits the left wall, as

expected by a meniscus that is not axisymmetric, but higher at the right wall than at the left wall.

### A.2.7. Tiny droplets

Figure 26 does not show bubbles at the free surface. It does show a spray of very small droplets which move up slightly faster than the jet. During one day of measurements this effect happened 90% of the time. Afterwards it was not observed anymore. This is likely caused by not completely removing the ethanol used to clean the tube, resulting in a sharply lower surface tension, which resulted in a more easy breakup of the surface.

## A.3. Schlieren Setup

Schlieren can be used to see density differences in a liquid, and since a pressure difference gives rise to a density difference it can be used to detect the pressure pulse. The principle it uses is that (local) density differences in the liquid create a change in the way the light gets refracted. A similar technique to Schlieren, shadowgraphy, occurs in daily situations, for an example when one looks at the shadow of hot air rising from a radiator. The difference between shadowgraphy and Schlieren is that whereas shadowgraphy visualizes the second spatial derivative, Schlieren visualizes the first spatial derivative. This means that Schlieren is more sensitive in most cases. We used a slightly adapted setup from Veldhuis (2006), see also his paper (chapter 2) for a more detailed explanation of the Schlieren setup. Difference with his setup is that in this research a stereoscopic setup is not used, since the pressure pulse is expected to be cylindrical symmetric. Different light sources are tried and also a raytracing program is used to check the setup.

To use the Schlieren setup to show pressure differences in a liquid that is contained by a tube, one should use ideally an index adapted liquid between the tube and a rectangular shaped box to make sure that the light does not get refracted too much at the tube's wall before reaching the interior of the tube. As seen in Zijlstra's master thesis, water might suffice as well. This is because the refractive index of water (1.33) is much closer to glass (1.40) than air (1) (Zijlstra, 2007)

### A.3.1. Light sources

During the setting up of the Schlieren it is found out that the type of light source makes a big difference. Therefore a small experiment is set up to find the best one. For this the Schlieren setup is made as seen in picture 27. Experimental parameters are the type of light source, the use of a focussing lens to get more light and the use of a diffusive plate. The test is done with the same camera that is used for displaying the shocktube, namely the Photron SA1. Also different camera lenses are used. As can be seen in picture 28, 2 distances are interesting, namely distance A - D (Aperture - Diffusive plate) and distance A - L (Aperture - Focussing Lens). To try the Schlieren setup, first a candle was used. To see density differences in

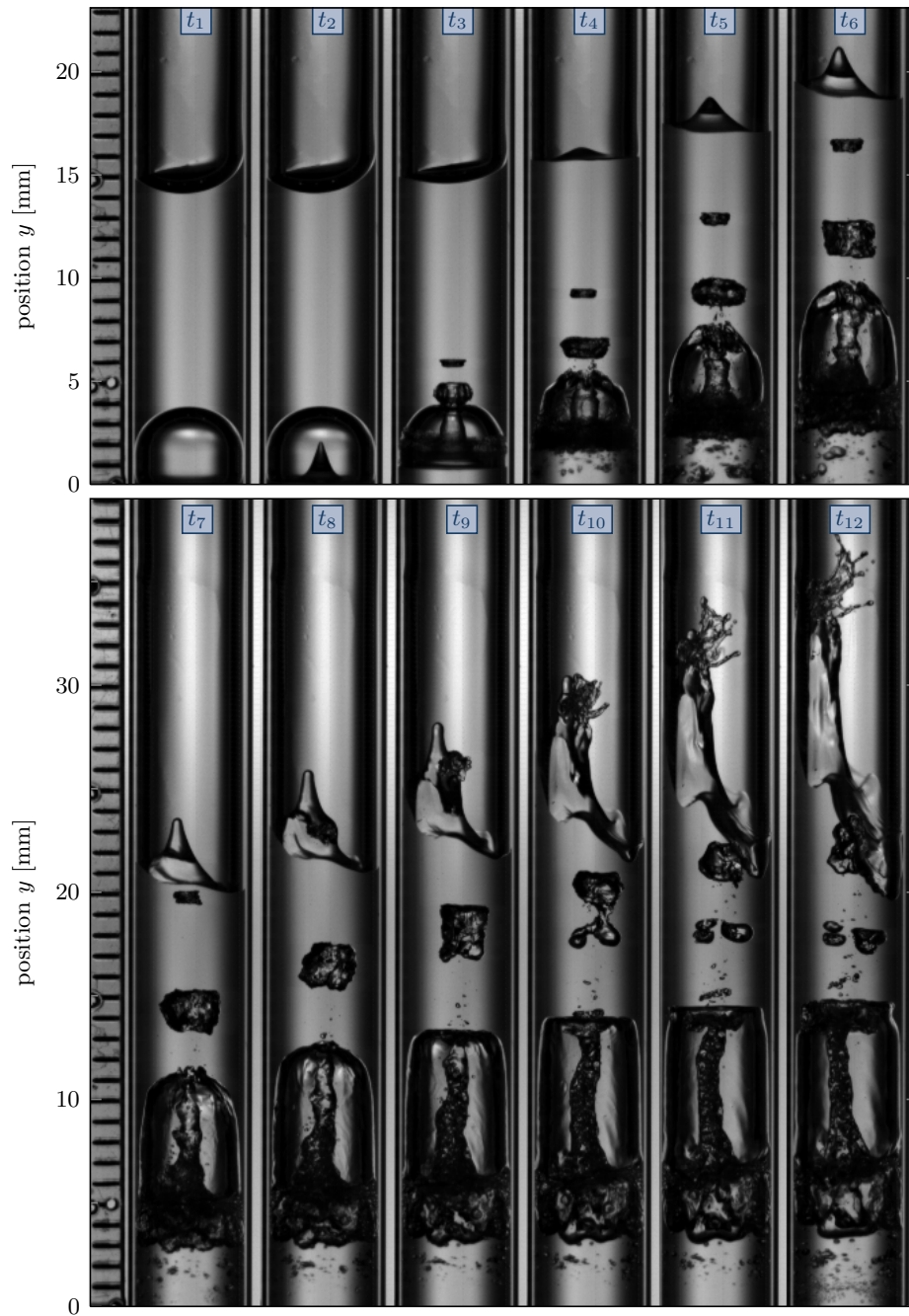


Figure 25: Image sequence as recorded by a high-speed camera at a framerate of  $40 \times 10^3$  FPS for an experiment with  $U_C = 2500$  V and  $d = 8$  mm (both representations are true to scale). The time interval separating each frame of this sequence is  $\Delta t = 0.225$  ms. The image sequence shows a big bubble about 1.5 cm below the surface. After the pressure pulse has hit, a jet is created inside this bubble.

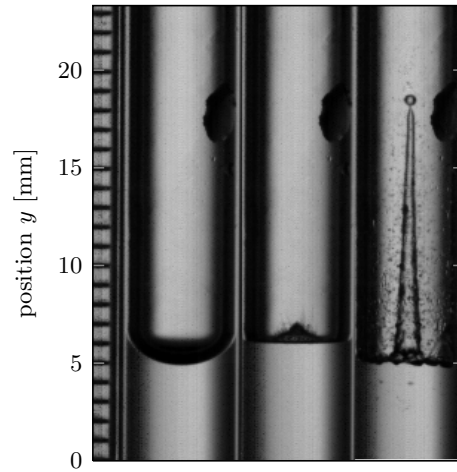


Figure 26: Image sequence as recorded by a high-speed camera at a framerate of  $17.5 \times 10^3$  FPS for an experiment with  $U_C = 1300$  V and  $d = 4$  mm. The interval between frame 1 and 2, and frame 2 and 3 are 0.11 ms and 0.19 ms, respectively.

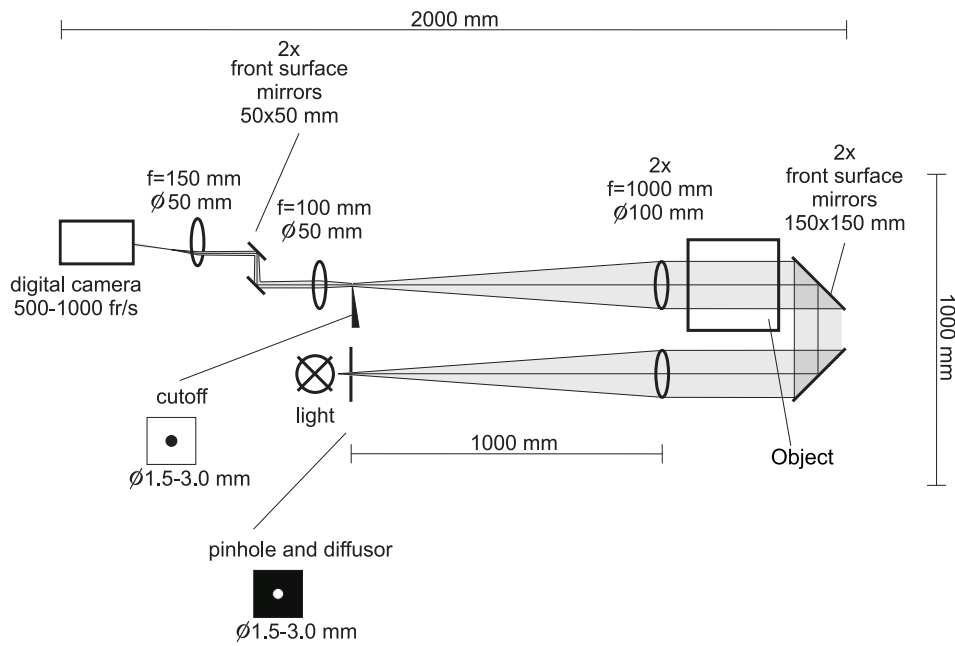


Figure 27: Experimental Schlieren setup. Figure adapted from Veldhuis (2006).

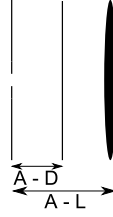


Figure 28: Schematic drawing of the light source

|                  | rms [nm] | peak-peak [nm] |
|------------------|----------|----------------|
| Uncleaned        | 3.4      | 25.8           |
| Ethanol/Nitrogen | 0.8      | 11.5           |
| Piranha          | 1.1      | 22.6           |

Table 4: The rms and peak-peak values for the three differently treated microscope slides.

air, created by a candle, an appropriate light source was the Sumita Halogen light (<http://www.sumita-opt.co.jp/>).

#### A.4. Cleaning method

Different cleaning methods are compared by Seddon<sup>3</sup>. Three microscope slides were given different treatments; no treatment, rinsed in ethanol after which they were dried in a dry-nitrogen stream, etched by piranha. Table 4 shows the rms and peak to peak values for the slides with different treatments obtained using a atomic force microscope. The peak-peak and rms value of the ethanol-nitrogen treatment is the lowest, therefore this is the preferred cleaning method, especially because it is also easier to perform then the piranha cleaning method. However, the piranha method results in a surface that is hydrophilic and might therefore bind the coating better. Figure 29 shows the scanned areas.

<sup>3</sup>James Seddon, PoF (J.R.T.Seddon@utwente.nl)

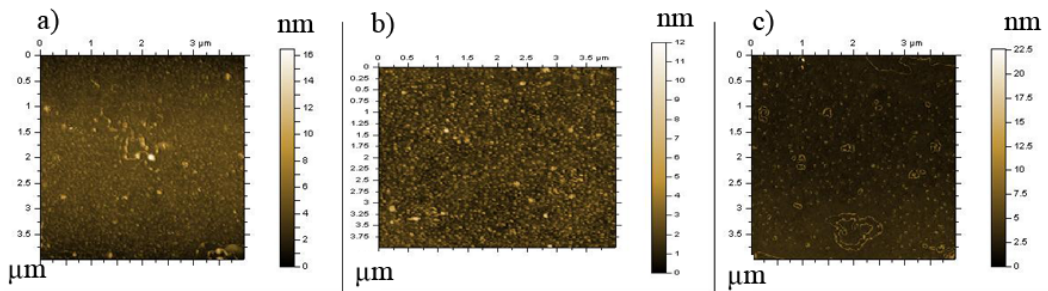


Figure 29: Different cleaning methods are shown, a) uncleaned, b) rinsed in ethanol, then dried in a nitrogen stream, c) cleaned using piranha. The images are 4 μm by 4 μm

